TÜRKİYE CUMHURİYETİ
ADANA ALPARSLAN TÜRKEŞ SCIENCE AND TECHNOLOGY UNIVERSITY

GRADUATE SCHOOL
MATERIALS ENGINEERING DEPARTMENT

FABRICATION AND CHARACTERIZATION OF TRANSITION METALS (Mn AND Co)-DOPED CdS-BASED PHOTOVOLTAIC CELLS

VOLKAN DOĞAN

M.Sc.

ADANA 2024

TÜRKİYE CUMHURİYETİ
ADANA ALPARSLAN TÜRKEŞ SCIENCE AND TECHNOLOGY UNIVERSITY

GRADUATE SCHOOL
MATERIALS ENGINEERING DEPARTMENT

FABRICATION AND CHARACTERIZATION OF TRANSITION METALS (Mn AND Co)-DOPED CdS-BASED PHOTOVOLTAIC CELLS

VOLKAN DOĞAN

M.Sc.

THESIS ADVISOR
PROF. DR. SALIH YILMAZ

ADANA, 2024

DECLARATION OF CONFORMITY

In this thesis study, which was prepared following the thesis writing rules of Adana Alparslan Türkeş Science and Technology University Institute of Graduate School, I declare that I provide all the information, documents, evaluations and results in accordance with scientific ethics and moral codes without resorting to any means or assistance that would be contrary to scientific ethics and traditions. I also declare that I refer to all of the articles I used in this study with appropriate references and accept all moral and legal consequences if a situation is found contrary to my statement regarding my work.

09/01/2024

Volkan DOĞAN

ÖZET

GEÇİŞ METALİ (Mn VE Co) KATKILI CdS TABANLI FOTOVOLTAİK HÜCRELERİN ÜRETİMİ VE KARAKTERİZASYONU

Volkan DOĞAN

Yüksek Lisans, Malzeme Mühendisliği Anabilim Dalı

Danışman: Prof. Dr. Salih YILMAZ

Ocak 2024, 61 sayfa

Bu çalışmada, kimyasal banyo yöntemiyle üretilen, hem Mn (%0.5, %1, %2) hem de Co (%1, %3, %5, %7) ile ayrı ayrı doplanmış CdS ince filmleri, indiyum kalay oksit (ITO) kaplı cam altlık üzerinde üretildi. Ek olarak N719, P3HT:PCBM ve PEDOT:PSS organik katmanları spin kaplama yöntemiyle birbirini takip edecek şekilde uygulanarak istenen cihaz konfigürasyonuna ulaşıldı. Mn ve Co içeren CdS ince filmlerin yanı sıra üretilen güneş hücreleri üzerinde kapsamlı XRD, SEM, EDS, geçirgenlik, absorpsiyon, PL analizleri gerçekleştirildi. Ayrıca üretilen cihazların J-V testleri de araştırıldı. XRD analizi ile üretilen CdS ince filmlerin kübik yapıda büyüdüğü görüldü. Mn atomlarının CdS yapısına eklenmesi, kristal kalitesinde kötüleşmeye işaret eden dislokasyon yoğunluğu ve mikro-gerilim sonuçları yardımıyla tespit edildi. Mn katkısının, CdS filmlerin geçirgenliği üzerinde olumlu bir etkisi olduğu görüldü. Özellikle %2 Mn katkılı CdS örneğinde 500-650 nm dalga boyu aralığında %90'dan fazla geçirgenlik elde edildi. Mn katkısı, CdS'nin yasak enerji bant aralığını artırdığı ve soğurma kenarında maviye doğru bir kayma oluştuğu belirlendi. Üretilen güneş hücrelerinin J-V ölçümlerinden, Mn katkısının CdS tabanlı hibrit güneş hücrelerinin verimliliğini artırdı görüldü. En yüksek güç dönüşüm verimliliğine % 2 Mn-katkılı CdS güneş hücresi ile ulaşıldı (%0.202). Co katkısı ise, CdS'nin birim hücre hacminde değişime ve CdS kristal boyutunda artışa neden oldu. Ayrıca Co katkısı ile CdS ince filmlerin tane boyutunda azalma meydana geldiği görüldü. Co katkısının CdS filmlerin optik geçirgenliğini artırdığı ve yasak enerji bant aralığını değiştirdiği görüldü. Photolüminesans sonuçlarına gelince, Co katkısının CdS filmlerinde ek kusur durumlarına neden olduğu tespit edildi. Co katkısının CdS tabanlı hibrit güneş hücrelerinin verimliliğini olumlu yönde etkilediği ve en yüksek verimlilik değerinin % 1 Co-katkılı CdS güneş pillerinden elde edildiği belirlendi (%0.488).

Anahtar Kelimeler: CdS ince filmler, Mn ve Co katkılama, kimyasal banyo biriktirme P3HT:PCBM, hibrit güneş hücresi

ABSTRACT

FABRICATION AND CHARACTERIZATION OF TRANSITION METALS (Mn AND Co)-DOPED CdS-BASED PHOTOVOLTAIC CELLS

Volkan DOĞAN

M.Sc., Department of Materials Engineering

Supervisor: Prof. Dr. Salih YILMAZ

January 2024, 61 pages

In this study, CdS thin films were produced via chemical bath deposition method, individually doped with Mn (0.5%, 1%, 2%) and Co (1%, 3%, 5%, 7%), on indium tin oxide (ITO) coated glass substrates. Additionally, the desired device configuration was achieved by coating N719, P3HT:PCBM, and PEDOT:PSS organic layers, respectively, using spin coating method. Comprehensive XRD, SEM, EDS, transmittance, absorbance, PL analyses were conducted on both Mn and Co-doped CdS thin films and the fabricated solar cells. Furthermore, J-V tests were performed on the fabricated devices. XRD analysis revealed that the produced CdS thin films grew in a cubic structure. Addition of Mn atoms into CdS structure was determined to deteriorate crystal quality based on dislocation density and micro-strain results. Mn doping led to a positive effect on transparency of CdS films, particularly achieving over 90% transmittance in the wavelength range of 500-650 nm for CdS sample with 2% Mn addition. Mn doping was found to increase forbidden energy band gap of CdS, causing a blue-shift in absorption edge. J-V measurements of the fabricated solar cells indicated that Mn doping improved the efficiency of CdS based hybrid solar cells. Highest power conversion efficiency was achieved with a 2% Mn-doped CdS solar cell (0.202%). On the other hand, Co doping led to a change in the unit cell volume and increase in crystalline size of CdS. Additionally, a reduction in grain size of CdS thin films was observed with Co doping. Co doping was found to enhance optical transparency of CdS films and alter the forbidden energy band gap. Photoluminescence results suggested that Co doping caused additional defect states in CdS films. Furthermore, Co doping positively influenced the efficiency of CdS-based hybrid solar cells, with highest efficiency obtained from solar cells with 1% Co doping (0.488%).

Keywords: CdS thin films, Mn and Co doping, chemical bath deposition, P3HT:PCBM, hybrid solar cell

ACKNOWLEDGEMENTS

I extend my deepest gratitude to my supervisor, Prof. Dr. Salih YILMAZ, for their invaluable guidance, continuous support, and insightful feedback throughout the completion of this thesis. Their expertise, encouragement, and unwavering dedication have been instrumental in shaping this work. I am also thankful for their patience and encouragement during the research process, which significantly contributed to the successful completion of this study. I also would like to express my gratitude to Research Assistant Saltuk Buğra TÖRELİ for his invaluable assistance and support during the laboratory studies. Additionally, my heartfelt thanks go to Prof. Dr. Murat TOMAKİN, who generously shared his knowledge during the analyses process of the samples, and to Prof. Dr. İsmail POLAT, who enlightened me with his expertise in the calculations of the collected data.

This work was supported by Scientific Research Projects Coordination Unit in Adana Alparslan Türkeş Science and Technology University under a grant number of 21303022. Author V.D. has received a scholarship from the Scientific and Technological Research Council of Turkey (TÜBİTAK) under 2210-C program with an application number of 1649B022203950.

TABLE OF CONTENTS

LIST OF FIGURES

LIST OF TABLES

LIST OF ABBREVIATIONS

CBD	: Chemical bath deposition
D-A	: Donor-Acceptor
DSSC	: Dye sensitized solar cell
EDS	: Energy dispersive spectroscopy
HOMO	: Highest occupied molecular orbital
ITO	: Indium tin oxide
LED	: Light-emitting diode
LUMO	: Lowest unoccupied molecular orbital
PCE	: Power conversion efficiency
PL	: Photoluminescence
PV	: Photovoltaics
RPM	: Revolutions per minute
RT	: Room temperature
RTPL	: Room temperature photoluminescence
SEM	: Scanning electron microscopy
Si	: Silicon
UV	: Ultraviolet
XRD	: X-Ray diffraction

LIST OF SYMBOLS

a	: Absorption coefficient
a	: Lattice parameter
Ag	: Silver
$CdCl_2$	: Cadmium Chloride
CdO	: Cadmium oxide
CdS	: Cadmium Sulfide
Co	: Cobalt
Cr	: Chromium
D	: Crystalline size
d	: Interplanar spacing
FF	: Fill factor
h	: Planck's constant
h, k, l	: miller indices
I_{Cd}	: Cadmium interstitial
I_S	: Sulphur interstitial
J_0	: Saturation current density
J_{max}	: Maximum power current density
J_{ph}	: Photo-generated current density
J_{SC}	: Short circuit current density
k	: Boltzmann constant
Mn	: Manganese
η	: Power conversion efficiency
N719	: cis-bis(isothiocyanato) bis(2,2-bipyridyl-4,4-dicarboxylato) ruthenium (II)
η_{abs}	: Absorption yield of the device
η_{cc}	: Efficiency of charge collection at the electrodes
η_{diff}	: Ability of an exciton to diffuse to a donor-acceptor interface
η_{diss}	: Exciton dissociation yield
NH_2CSNH_2	: Thiourea
NH_4Cl	: Ammonium chloride
NH_4OH	: Ammonia solution (25%)
η_{tr}	: Efficiency of charge carrier transport throughout the device

P3HT	: poly(3-hexylthiophene-2,5-diyl)
PCBM	: phenyl-C61-Butyric-Acid-Methyl Ester
PEDOT:PSS	: poly(3,4-ethylenedioxythiophene) polystyrene sulfonate
P_{in}	: Incident input power
q	: Electric charge
Sc	: Scandium
T	: Temperature
Ti	: Titanium
TiO_2	: Titanium dioxide
UV	: Ultraviolet
V	: Vanadium
ν	: frequency of light
V_{Cd}	: Cadmium vacancies
V_{max}	: Maximum power voltage
V_{OC}	: Open circuit voltage
V_S	: Sulphur vacancies
ZnO	: Zinc oxide
β	: Full width at half-maximum
δ	: Dislocation density

1. INTRODUCTION

1.1. Solar Cell Applications: An Overview

Due to growing population and developing technology, today's world has a constant need for energy. Importance of renewable energy and studies in this direction are also continuously increasing because of gradual decrease of fossil fuels used in traditional energy production, their unsustainability and damage they cause to the environment. Increasing global concerns about climate change and the predicted increases in global energy consumption have focused research attention on renewable and clean energy sources such as solar energy (Wright & Uddin, 2012).

Photovoltaics (PV) is a system comprised of cells that generate electricity from sunlight. Each cell contains semiconductor layers; when sunlight interacts with cell, it creates an electric field between these layers, resulting in flow of electricity. Researches on semiconductor-based solar cells have been ongoing for 80 years, and new developments continue to be made. (Tyagi et al., 2013). Silicon solar cells currently dominate photovoltaic market due to their superior charge transfer capabilities and environmental stability. Power conversion efficiencies (PCE) up to 25% have been demonstrated. PV has grown rapidly over during the past decade, but higher energy prices compared to traditional generation methods have prevented PV from delivering a significant amount of steady-state energy to the world. On the other hand, high costs associated with silicon purification methods have diminished enthusiasm for silicon-based solar cells. Thin-film solar cells represent an innovative approach to photovoltaics. They offer considerable design flexibility and production methods that can be tailored to specific requirements. These cells consist of multiple layers with thicknesses ranging from nanometers to micrometers. One of the key advantages of thin film solar cells over traditional wafer-based solar cells is their cost-effectiveness and production flexibility. As a result of these advantages, they have aroused significant attention in recent researches. (Chen et al., 2013). According to the different types of materials utilized, solar cells have been grouped into three primary categories which consist of hybrid, organic-organic, and inorganic-inorganic solar cells (Wright & Uddin, 2012).

1.2. Hybrid Solar Cells

Hybrid solar cells have a potential to yield more promising devices harnessing the advantages of both organic and inorganic materials and it gains more popularity in terms of scientific aspects (Cortina et al., 2012). Production and operational principles of hybrid solar cells closely resemble those of organic solar cells, with primary distinction being the selection of an inorganic material as electron acceptor. Inorganic materials offer favorable attributes, including high optical transmittance, superior charge carrier mobility, environmental stability. Conversely, flexibility, improved surface morphology, and cost-effectiveness of organic materials have served as key drivers behind exploration of hybrid solar cell (Tyagi et al., 2013).

1.3. Working principle of hybrid solar cells

When incident light interacts photoactive layer, it results in the formation of an excited state. However, electron and holes are bound coulombically. This coupled electron-hole pair is referred to as "exciton." Overcoming exitonic binding energy necessitates application of a specific force, which facilitates production of free charge carriers capable of being transported throughout entire device. In the context of hybrid solar cells, excitons, initially formed within the donor material, go through separation at the donor-acceptor (D-A) interface. Force essential to surpass excitonic binding energy is provided by energy level offset between the lowest unoccupied molecular orbital (LUMO) of donor and conduction band's edge in the acceptor materials. Energy offset employed for dissociation of excitons is representing the excited state energy offset and indicated as ΔE_{ES} in Figure 1.1. In order to occur separation of excitons formed within acceptor material, it is imperative to consider energy offset between the highest occupied molecular orbital (HOMO) of donor and the valence band edge of acceptor materials. This particular energy offset for exciton dissociation is represented as ΔE_{GS} in Figure 1.1. (Wright & Uddin, 2012).

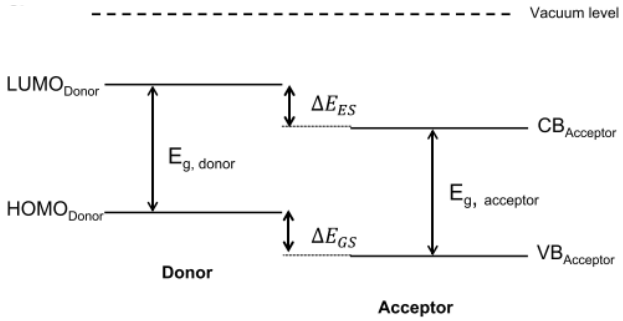

Figure 1.1. Energy band diagram of heterojunction solar cell (Wright & Uddin, 2012)

Excitonic dissociation takes place at the interface between donor and acceptor phases due to the energy offset. Subsequent to this separation, electrons are gathered at the cathode, a process termed charge collection. Holes generated as a result of this phenomenon migrate towards the anode where they accumulate (Chandrasekaran et al., 2011).

When electron-hole pair dissociates in the donor material, electrons move from donor-acceptor interface towards the acceptor material and are transported to the cathode. Simultaneously, holes move towards anode. Inorganic acceptor materials can contribute to the photocurrent. Upon the dissociation of excitons resulting from the absorption of light by the acceptor, the holes are transferred from donor-acceptor interface to donor and move towards anode, while electrons move towards cathode. Both of these scenarios are illustrated in Figure 1.2. (Wright & Uddin, 2012).

Consequently, precise arrangement of donor-acceptor materials within active layer holds paramount significance for effective operation of device. Limited excitonic diffusion length significantly constrains feasibility of bilayer structures. This limitation implies that free charge carriers can only be generated in response to photoexcitation at the interface falling within the range of exciton diffusion length. To boost interfacial area and enhance excitonic dissociation, it is possible to create a structure referred to as a bulk heterojunction device by blending the donor and acceptor materials (Wright & Uddin, 2012). A device featuring a substantial dispersion of interfaces within the photoactive layer necessitates shorter exciton diffusion distances. As a result, a more exciton dissociation yield is occurred. However, there is a thin line between enhancing interfacial area through the close distribution of phases and establishing efficient pathways for transport of free electrons and holes. Thus, precise arrangement of donor and acceptor phases significantly influences device's performance (Hau et al., 2010; Wright & Uddin, 2012).

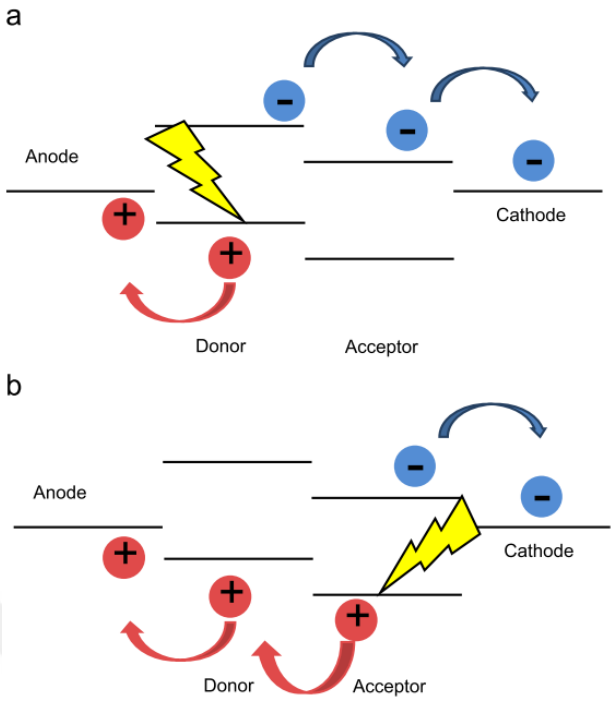

Figure 1.2. Schematic representation of charge transfer for (a) photogeneration in electron donor, (b) photogeneration in the electron acceptor (Wright & Uddin, 2012)

1.4. Performance Characteristics

1.4.1. Power conversion efficiency (PCE, η)

Measurement of power generated by a solar cell relative to the power of incident solar radiation is termed as power conversion efficiency. J_{SC} is short circuit current density, V_{OC} is open circuit voltage, FF is fill factor and P_{in} encompasses the summation of all wavelengths and is typically standardized at 1000 W/m² in the context of solar simulator applications at room temperature (Chandrasekaran et al., 2011).

$$PCE = \frac{J_{SC} \times V_{OC} \times FF}{P_{in}} \quad (1.1)$$

Hence, there exist three key device characteristics that collectively ascertain the efficiency of device. Subsequent topics enlightens the factors that influence these device characteristics in the context of organic-inorganic hybrid solar cells.

1.4.2. Short circuit current-density (J_{SC})

When cell operates at a short circuit, voltage becomes 0. Thus, current flowing through the cell is defined as short-circuit current. J_{SC} known as short circuit current-density is closely associated with external quantum efficiency. External quantum efficiency represents the proportion of collecting photogenerated electrons to the number of incident photons at a particular wavelength. Relationship between J_{SC} and external quantum efficiency can be explained by the following equation;

$$Jsc=\frac{q}{hc}\int_{\lambda_{min}}^{\lambda_{max}} EQE\times P_{in}(\lambda)\lambda \times d\lambda \quad (1.2)$$

In the functioning of a hybrid solar cell, this metric relies on five key steps, each characterized by its respective efficiency. As a result, external quantum efficiency can be written as following;

$$EQE= \eta_{abs}\times\eta_{diff}\times\eta_{diss}\times\eta_{tr}\times\eta_{cc} \quad (1.3)$$

Here, η_{abs} denotes absorption yield of the device, which stands as the most influential factor for enhancing J_{SC} value of the device. Material's absorption spectrum is influenced by both band gap and absorption coefficient of the material. Additionally, absorption yield is influenced by thickness of the active layer. η_{diff} represents the capability of an exciton to diffuse to a D-A interface. This ability relies on two factors: excitonic diffusion length, which is an inherent material property, and distance between excitation and nearest interface. η_{diss} represents exciton dissociation yield. Since electron remains bound within the exciton, an energy offset is essential at D-A interfaces to induce a driving force that releases electron, enabling conduction. For effective charge transfer, this energy offset must exceed excitonic binding energy in the material, typically falling within the range of 0.1–0.5 eV. η_{diss} characterizes efficiency of charge carrier transport within the device. In organic materials, transport of charges involves a hopping process between energy states and is influenced by traps and recombination sites within the photoactive film. Effect of this transport is significantly dependent on the mobility of respective semiconductors. Parameter η_{diss} characterizes efficiency of charge collection at electrodes, reflecting the ability of charge carriers to be introduced into electrodes from the photoactive layer. Success of this process heavily relies on electronic configuration of device. To ensure effective injection of electrons into cathode, conduction band edge energy level of acceptor

material, relative to the vacuum level, must be lower than that of the work function of the metal. Likewise, for successful injection of holes into anode, the highest occupied molecular orbital level of donor material must exceed work function of transparent anode. All these terms are depicted schematically in Figure 1.3. (Wright & Uddin, 2012).

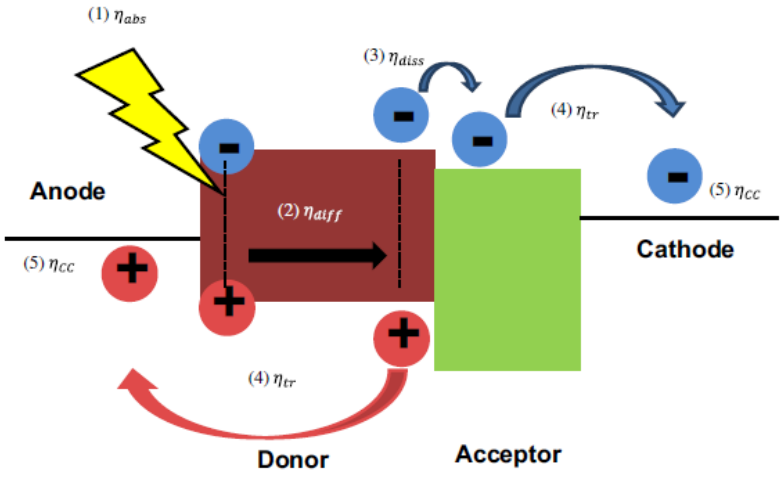

Figure 1.3. Illustration of five key steps in the charge transfer phenomena (Wright & Uddin, 2012)

1.4.3. Open circuit voltage (V_{OC})

During operation at open circuit conditions, when current is equal to zero, voltage across the output terminals is defined as open circuit voltage. It can be expressed mathematically as the following relation,

$$V_{OC} = \frac{k \cdot T}{q} \ln\left(\frac{J_{ph}}{J_0} + 1\right) \tag{1.4}$$

where k represents Boltzmann constant, *T* signifies temperature, q denotes charge, J_{ph} accounts for the photogenerated current, and J_0 corresponds to saturation current density (Chandrasekaran et al., 2011).

1.4.4. Fill factor

This refers to a ratio of the maximum power to the product of open-circuit voltage and short-circuit current and is indicated by an equation;

$$FF=\frac{J_{max}\times V_{max}}{J_{SC}\times V_{OC}} \quad (1.5)$$

where J_{max} and V_{max} represent maximum power current density and voltage, respectively, while J_{SC} is short-circuit current density, and V_{OC} is open-circuit voltage. The ratio described above is depicted in Figure 1.4. Due to inherent limitations on diode quality, practical fill factor is constrained to be less than ideal value of 1. Behavior of an actual diode deviates from ideal, primarily due to recombination events occurring at the junction. In the case of organic photovoltaic and hybrid solar cells, the 'junction' is represented by D-A interface, distributed throughout the entire photoactive layer. Quantitative characterization of deviations from ideal case, and consequently the shape of current-voltage (J-V) curve, can be achieved by considering parasitic loss mechanisms of series and shunt resistance. An ideal scenario involves zero series resistance; however, poor conductivity across active layer and reduced charge carrier injection to electrodes contributes to the increased series resistance. On the contrary, ideal diode scenario demands infinite shunt resistance, but imperfections within the photoactive film or current leaks at the interface between layers in device lead to a reduction in shunt resistance. Figure 1.4. visually illustrates the relationship between V_{OC}, J_{SC}, J_{max}, V_{max}, and the fill factor, depicting the electrical parameters of the material. (Wright & Uddin, 2012).

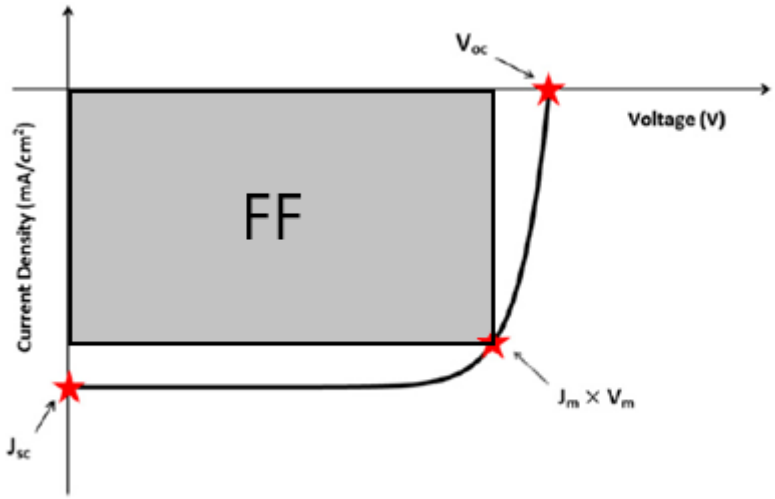

Figure 1.4. General current density-voltage curve for a solar cell describing J_{SC}, V_{OC}, J_{max}, V_{max} and FF.

1.5. Doping in inorganic semiconductors

Initial exploration of semiconducting materials and notably, the groundbreaking advancement in manipulating their electrical characteristics through a process known as doping, laid the foundation for a lot of electronic devices commonplace in today's information-driven society. Doping of inorganic semiconductors facilitates the modification of energy alignment of their electronic bands concerning metal contacts and other differentially doped semiconductors. Interfacial phenomena, observed in structures like p-n junctions or field-effect transistors, backs up the diverse functionalities harnessed in silicon-based electronics.

Doping treatment of inorganic material involves adding impurity atoms to a pure semiconductor, creating electronic defect states in fundamental band gap. For p-type doping, electron chemical potential shifts downward, with deliberately shallow acceptor states occupied, leading to mobile holes. N-type doping introduces intentionally placed shallow donor states below conduction band edge, resulting in mobile electrons. This efficient process significantly enhances semiconductor conductivity, even at low doping ratios, while maintaining high charge carrier mobility due to minimal disruption of host's crystal structure (Salzmann et al., 2016).

It is evident that doping utilizes a noticeable influence on structural, morphological, optical, magnetic, and mechanical properties of the material, in addition to its impact on the aforementioned electronic properties. Introduction of impurity atoms induces notable alterations across multiple material characteristics, emphasizing the intricate interplay between doping and diverse physical and electronic attributes of the material.

2. LITERATURE REVIEW

In this comprehensive literature review, we commence by examining pertinent studies focusing on CdS thin film-based solar cells, investigating their integration with notable materials such as N719, P3HT:PCBM, and PEDOT:PSS layers. Subsequently, we delve into exploration of research to clarify the impacts of cobalt and manganese doping on CdS thin films. This section aims to provide an understanding of how these dopants influence the structural and optoelectronic properties of CdS, shedding light on their potential enhancements. Finally, we analyze works that explore photovoltaic characteristics originating from the optimization processes and device configurations of CdS thin films.

Among semiconductor compounds belonging to II-VI group, CdS stands out as a popular n-type inorganic material. It possesses distinctive characteristics such as low resistivity, high stability, a moderate band gap of 2.42 eV at room temperature, and good electron mobility (Prabahar & Dhanam, 2005). These properties have led to the widespread use of CdS in various applications, including LEDs (Pradeep et al., 2016), sensors (Du et al., 2014) transistors (Wondmagegn et al., 2016), photodetectors (Deng & Li, 2014), and solar cells (Yılmaz, Ünverdi, et al., 2020). Growth of CdS thin films can be achieved through multiple methods, including thermal evaporation (Jassim et al., 2013), pulsed laser deposition (Martínez-Landeros et al., 2019), spray pyrolysis (Hiie et al., 2006), and chemical bath deposition (CBD) (Khallaf et al., 2008).

CBD stands out as a straightforward and cost-effective production method, enabling deposition at low temperatures and even over large areas. This technique has been employed in the production of CdS thin films since 1960's (Khallaf et al., 2008). Furthermore, CdS thin films, fabricated through CBD method, have aroused interest in solar cell researches. Yılmaz and his colleagues studied the use of CBD-grown CdS thin films for hybrid solar cell applications, focusing on surface modification by some diverse dyes. The reported study revealed the potential use of a few dyes for exhibiting photovoltaic characteristics and demonstrated a possibility of enhancing device's efficiency by surface modification by N3 dye. Devices manufactured in the study exhibited efficiencies ranging from 0.045% to 0.322%, displaying variations based on the surface modifications. (Yılmaz et al., 2019). Additionally, El-Shaer and co-workers deposited CdS thin films on glass slides using chemical bath deposition. They

investigated the impact of deposition time through various analyses, it was found the formation of both cubic and hexagonal structures in CdS thin films, with crystallite sizes ranging from 21 to 50 nm. SEM results displayed hierarchical nanoparticles. Raman studies confirmed distinctive vibration modes, and UV-Vis spectra indicated absorption edges near 500 nm, correlating with CdS band gap. Estimated band gap decreased from 2.4 to 2.22 eV with the increased deposition time. PL results revealed a main peak at 537 nm and its intensity decreased with increasing deposition time, suggesting a reduced charge carrier recombination. These all findings highlight that CdS thin films are promising materials for optoelectronic applications (El-Shaer et al., 2023).

Fabrication of doped and undoped CdS-based hybrid solar cells provides key components, namely N719, P3HT:PCBM, and PEDOT:PSS layers, influencing overall device performance. Utilization of these three organic materials in solar cell applications has been a focal point in recent studies. Thitima and co-workers highlighted positive impact of N719 dye in surface modification. In this paper, primary focus was to advance hybrid solar cells through the combination of metal oxides with high electron mobility and organic semiconductors, particularly conjugated polymers. The study illustrated the enhanced charge injection efficiency of a hybrid solar cell, comprising poly(3-hexylthiophene) (P3HT) and (6,6)-phenyl C61 butyric acid methyl ester (PCBM)/ZnO, with and without incorporation of N719 dye molecule. Modification of ZnO nanorod arrays with N719 resulted in a significant increase in short-circuit current density (J_{SC}) to 8.89 mA/cm^2, representing a 1.5-fold improvement compared to the configuration without N719. Moreover, power conversion efficiency exhibited a noteworthy enhancement, rising from 1.16% to 2.0%, credited to additional surface modification of ZnO nanorod array with N719 dye (Thitima et al., 2009). On the other hand, P3HT:PCBM, a component of organic layers in designed solar cell, is widely recognized and highly suitable for organic-based photovoltaic (PV) studies. Dang et al. investigated that in the field of polymer-based photovoltaic cells, P3HT:PCBM emerged as the most extensively investigated active materials globally for bulk-heterojunction structure. Various power-conversion efficiencies were documented, reaching levels of approximately 5%. They also devoted to reviewing substantial literature published between 2002 and 2010, with a specific focus on solar cells utilizing blends of P3HT:PCBM (Dang et al., 2011). In addition, Yavuz et al. investigated the photovoltaic performance analysis of inverted structure hybrid solar cells, which were fabricated using CdS films and a photoactive layer consisting of P3HT:PCBM. Deposition of

CdS thin films with varying thicknesses was carried out utilizing the spray deposition technique. Current–voltage characteristics were measured under both dark and AM 1.5 illumination (mW/cm^2) conditions. In the inverted structure of hybrid solar cells employing CdS thin films, a short circuit current density of 1.9 mA/cm^2 was achieved, resulting in a power conversion efficiency of approximately 0.3% (Yavuz et al., 2013). Numerous studies in the literature have explored that a PEDOT:PSS was used an additional organic material layer in designed solar cell. For example, Shi et al. conducted a comprehensive review on optical, electrical, and chemical characteristics of PEDOT:PSS. They studied organic material in terms of its conductivity, high transparency, favorable film-forming properties, and thermal stability. Their findings suggested that PEDOT:PSS was highly compatible and suitable material for solar cell research (Shi et al., 2015). Moreover, Kadem and co-workers conducted a work on examination of the optical transmittance, electrical conductivity, and morphology of PEDOT:PSS treated with ammonium hydroxide (NH_4OH). Transmittance spectra of spun PEDOT:PSS layers revealed a slight enhancement with increasing of ammonium hydroxide in addition to the film surfaces displaying variations in roughness and an increase in electrical conductivity. Enhancement in the physical properties of PEDOT:PSS was identified as a pivotal factor contributing to the improvement in power conversion efficiency (PCE), reaching values as high as 4%. It is noteworthy to mention that untreated form of PEDOT:PSS also exhibited good photovoltaic characteristics in the study (Kadem et al., 2018).

As mentioned in the previous section of the thesis, doping is a widely used method in semiconductor materials and their applications and allows material to be tuned as desired. Motivation of this study originates from literature review, which revealed absence of studies on doping of Mn and Co elements into CdS within the designed device configuration. In contrast, existing articles delved into the doping processes of these elements into CdS thin films, exploring their electrical, optical, and morphological effects on CdS. Balpınar et al. fabricated dye-sensitized solar cells (DSSCs) using murexid dye and manganese-doped cadmium sulfide (CdS:Mn) thin films. CdS:Mn films synthesized on ITO coated glass substrates via chemical bath deposition. Manganese doping concentrations ranged from 0% to 6%. Structural, morphological, and optical properties were analyzed using XRD, AFM, and UV–visible absorption spectrometry. J-V curves assessed the impact of nanoparticle size on DSSC performance, revealing a maximum efficiency of 3.40%. These results suggested that CdS:Mn heterojunction holds promising material for DSSC applications, aligning with the objectives of

this work (Balpinar, 2020). Furthermore, Suo and co-workers conducted an investigation on the impact of transition metals (Sc, Ti, V, Cr, and Mn) doping on the electronic structure and optical properties of CdS. It revealed that Mn doping led to an increasedin the conductivity and carrier mobility. Additionally, Mn doping enhanced the absorption of CdS in the visible light of spectrum, indicating a desirable material for solar cell applications (Suo et al., 2020). Another study related to this topic was conducted by Jabeen et al. where CdS and Mn-doped CdS nanocrystals were synthesized using the co-precipitation method. Nanocrystals extensively were characterized through various techniques. Addition of Mn impurity in CdS lattice induced a significant blue shift in absorption band, leading to a reduction in nanocrystal size. Band gap alteration, attributed to the quantum confinement effect, ranged from 2.11 to 2.21 eV as Mn incorporation was varied in CdS. Morphology and packing behavior of blend of nanocrystals with the organic polymer were studied using Atomic Force Microscopy. Additionally, synthesized nanomaterial, when combined with P3HT, was utilized in the construction of photovoltaic cells. Power conversion efficiency of these devices enhanced by incorporation of Mn impurity in CdS lattice, demonstrating a good potential for the improved performance in photovoltaic applications (Jabeen et al., 2018). Aksay and co-authors studied the structural, optical and vibrational properties of Co doped CdS films. An ultrasonic spray pyrolysis approach was used to deposit CdS and CdS/Co films on glass substrates. They found that Co doping decreased band gap of CdS from 2.42 eV to 2.39 eV (Aksay et al., 2011). Giribabu and co-workers also investigated CdS and Co-doped CdS films fabricated on glass substrates utilizing the ultrasonic spray pyrolysis method. The report systematically explored the influence of Co incorporation on structural, optical, morphological, elemental, and vibrational characteristics of these films. XRD analysis proved the hexagonal wurtzite structure in all films, demonstrating the absence of impurity phases. A decrease in direct optical band gap from 2.42 to 2.39 eV was observed with rising of Co incorporation. This reduction in energy gaps was primarily ascribed to the sp–d exchange interaction between the localized d-electrons of Co^{2+} ions and band electrons of CdS. Optical assessments further revealed a decline in transmittance of CdS films as the Co content increased (Giribabu et al., 2013). Finally, Firoozi et al. conducted a research on investigating influence of Co^{2+} ion incorporation into CdS layer on the photovoltaic performance of a quantum dot sensitized solar cell. CdS quantum dots were deposited onto mesoporous TiO_2 film using the successive ionic layer adsorption and reaction method. Co-doping altered the structure of photoanode, leading to an increase in short-circuit current density. Electrochemical impedance analysis indicated a reduction in charge transfer

resistance at TiO_2/quantum dots/electrolyte interface due to the presence of an internal recombination pathway. A highest energy conversion efficiency (η) of 3.16% was achieved under simulated sunlight by doping of the optimized amount of Co^{2+} ions in CdS nanoparticles. This resulted in a 35% increase in efficiency compared to undoped device, attributed to the superior of charge collection over recombination (Firoozi et al., 2015).

Following an extensive literature review, a comprehensive understanding has been developed, shaping direction of the study. CdS, as an inorganic material, emerges as a promising candidate for solar cell applications. Chemical bath deposition method stands out for its cost-efficiency and simplicity, establishing it as a widely adopted technique. Other organic layers have gained popularity in solar cell research, with ongoing efforts to enhance their properties. Literature reveals promising outcomes from doping effect, particularly with selected elements like Mn and Co, improving the electrical and optical characteristics of CdS thin films. Notably, identified device configuration lacks precedent in existing literature, emphasizing novelty and potential value of exploring this path in the study. In light of these research findings, it becomes clear that delving into this unique hybrid solar cell configuration is a valuable and worthwhile pursuit.

This research aims to systematically investigate fabrication and performance evaluation of chemical bath-grown CdS thin films, both undoped and individually doped with Mn and Co atoms on indium tin oxide (ITO) substrates. Primary objectives encompass the growth of CdS thin films, subsequent deposition of N719, P3HT:PCBM and PEDOT:PSS organic layers using spin coating method, and construction of solar cell devices. Study further focuses on conducting comprehensive XRD, SEM, EDS, transmittance, absorbance, photoluminescence (PL), and J-V analyses on both undoped and doped CdS thin films and their devices. Investigation specifically intends to determine the structural, morphological, and optical properties of CdS films with Mn and Co doping, providing insights into crystal quality, grain morphology, transparency, and band gap variations. Moreover, our purpose is to compare the photovoltaic efficiencies of CdS-based devices, highlighting the role of Mn and Co dopants in enhancing overall device performance. Possible outcomes contribute to the understanding of how Mn and Co doping influence the characteristics of CdS thin films and their subsequent impact on the efficiency of solar cell devices, providing valuable insights for advancement of hybrid solar cell technology. Mn atoms are chosen as 0, 0.5, 1 and 2 % in CdS structure while concentration of

Co atoms is selected as 1, 3, 5 and 7 %. Schematic representation of the planned device configuration is presented in the Figure 2.1.

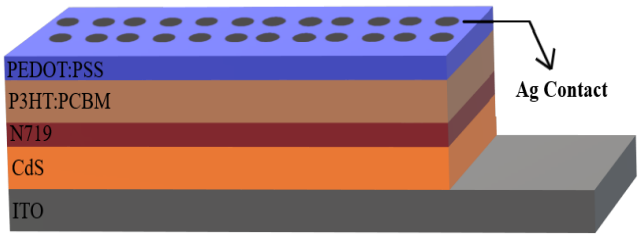

Figure 2.1. Schematic illustration of the planned device.

3. MATERIALS AND METHODS

3.1. Chemical Bath Deposition

Chemical bath deposition stands out as one of the most straightforward solution-based methods for preparing thin films from aqueous solutions (Kathalingam, 2010). In this technique, thin films are deposited onto appropriate substrates by immersing them in a dilute solution containing metal ions, a source of hydroxide, sulfide, or selenide ions, and other necessary components (Nair, 1998). In addition to its simplicity, this technique offers several advantages. By manipulating solution parameters such as pH, temperature, and bath concentration, it allows for precise control over crucial thin film characteristics, including film thickness, deposition rate, and crystal quality. Furthermore, this method does not necessitate high-voltage equipment, can be employed at temperatures near room temperature, and proves to be relatively cost-effective (Kathalingam, 2010). Schematic representation of chemical bath deposition method is illustrated in Figure 3.1.

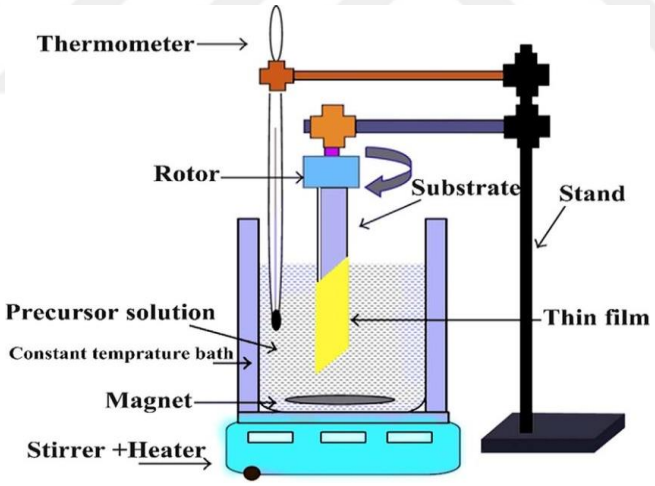

Figure 3.1. Schematic diagram of chemical bath deposition (Dive et al., 2018).

3.2. Production of CdS, Mn-doped CdS and Co-doped CdS thin films by CBD Method

ITO substrates were cut to 1.5 cm x 1.25 cm in size. ITO substrates were sequentially cleaned in an ultrasonic bath with acetone, ethanol and distilled water for 15 mins each. Cleaned ITO substrates were dried by nitrogen gas and the parts of the substrates that should not be coated (back side and contact area) were covered with Teflon and prepared for CBD process. In the

production of undoped CdS thin films, solutions of 0.02 M $CdCl_2$ in distilled water of 20 ml, 0.05 M thiourea (CH_4N_2S) in distilled water of 20 ml, 0.05 M NH_4Cl in distilled water of 20 ml, 1 ml distilled water and 14 ml %25 NH_4OH solution were prepared. For manganese and cobalt doping, 0.02 M $MnCl_2 \cdot 4H_2O$ and 0.02 M $CoCl_2 \cdot 6H_2O$ were added to the solution separately to obtain Mn-doped and Co-doped CdS thin films. Then, solution was transferred to the beaker for CBD process. The cleaned ITOs were immersed in the solution and were started to be heated from room temperature to 75 °C about 3 h and kept at this temperature for 30 mins. After CBD process, samples were removed from the solution and cleaned the surface of them with distilled water and ethanol to get rid of undesired particles. The obtained undoped, Mn-doped (0.5%, 1% and 2%) and Co-doped (1%, 3%, 5% and 7%) CdS thin films grown on ITO substrates were shown in Figure 3.2, respectively.

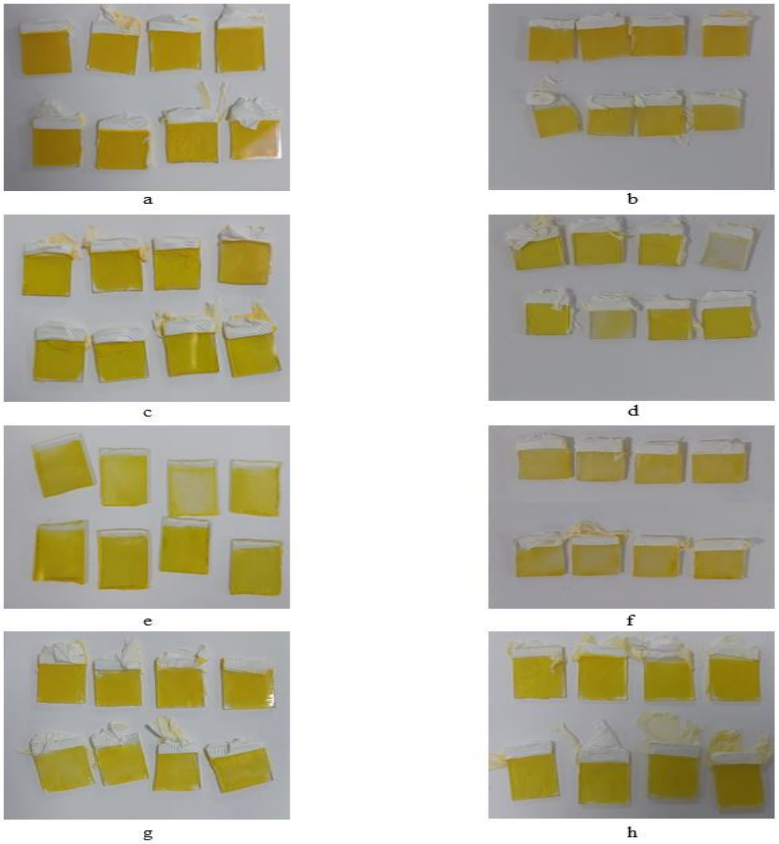

Figure 3.2. (a) undoped CdS and (b) 0.5% Mn, (c) 1% Mn, (d) 2% Mn, (e) 1% Co, (f) 3% Co, (g) 5% Co, (h) 7% Co doped CdS thin films.

3.3. Spin Coating Method

Spin coating stands out as the predominant method employed to produce uniform thin films of photosensitive organic compounds, ranging in thickness from micrometers to nanometers. The origin of spin coating can be traced back to the utilization of materials such as paint and pitch. This process comprises several distinct stages, including fluid distribution, spinning, a consistent fluid outlet flow, and ultimately, drying dominated by evaporation. Among these stages, flow control and evaporation management are paramount, significantly influencing the final coating thickness (Sahu & Panigrahi, 2009). Thin films of organic materials (N719, P3HT, P3HT:PCBM, PEDOT:PSS) in this study were produced using the spin-coating process with a Laurell WS-650 model spin coater. The device is illustrated in Figure 3.3

Figure 3.3. Laurell WS-650 model spin coater device.

3.4. Surface Modification of undoped and doped CdS Thin Films with N719 Dye

0.5 mM N719 dye was dissolved in pure ethanol to prepare the desired solution. Undoped and doped CdS thin films were kept in this solution for 24 h to achieve a coating of N719 dye. Then, samples were taken from the solution and prepared for the spin coating process. N719 solution was applied to each samples 10 times at one minute intervals at 1000 rpm. Top view pictures of N719 dye coated samples of undoped, Mn-doped (0.5%, 1% and 2%) and Co-doped (1%, 3%, 5% and 7%) CdS thin films were shown in Figure 3.3, respectively

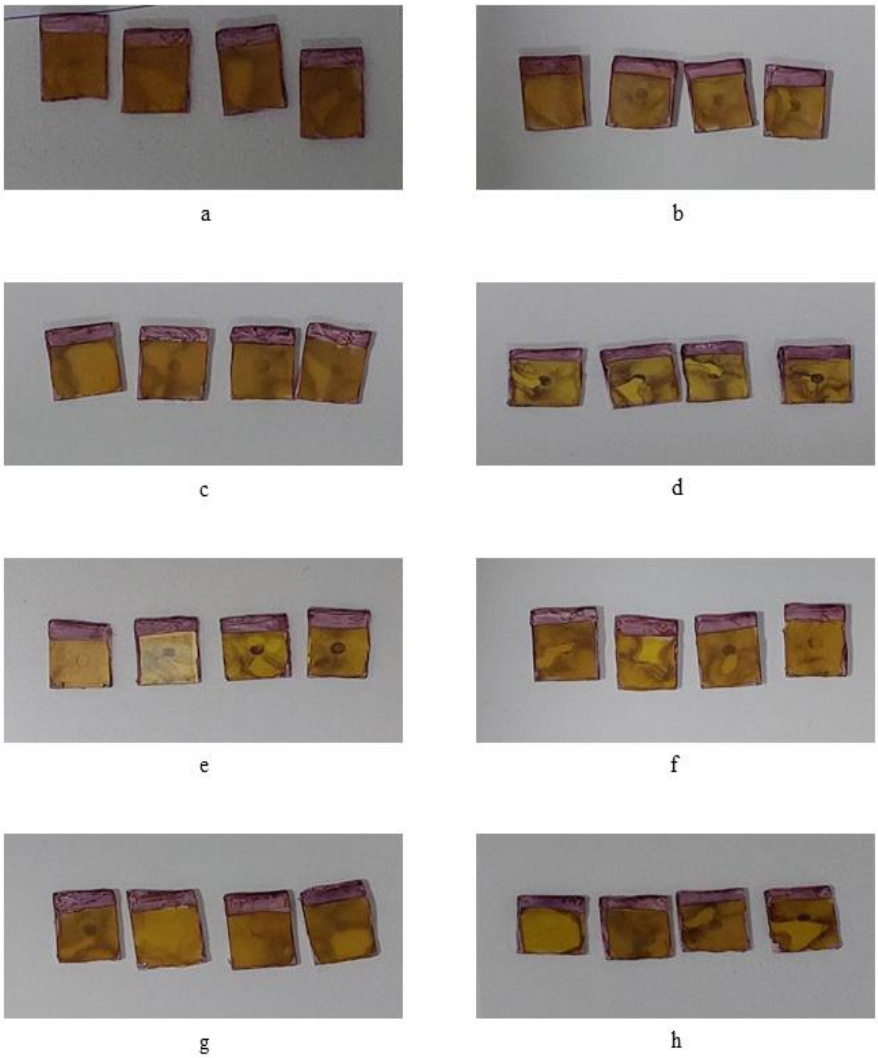

Figure 3.4. (a) undoped CdS and (b) 0.5% Mn, (c) 1% Mn, (d) 2% Mn, (e) 1% Co, (f) 3% Co, (g) 5% Co, (h) 7% Co doped CdS thin films with N719 layer.

3.5. P3HT and P3HT:PCBM Layers Produced by Spin Coating Method

Two types of solution were prepared for obtaining P3HT and P3HT:PCBM blend layers in the study. First, 0.1 g of P3HT polymeric material was dissolved in 5 ml of chlorobenzene. Then, solution was applied to each sample 5 times at 1 minute intervals at 1000 rpm. The obtained images of undoped, Mn-doped (0.5%, 1% and 2%) and Co-doped (1%, 3%, 5% and 7%) CdS thin films were shown in Figure 3.4, respectively.

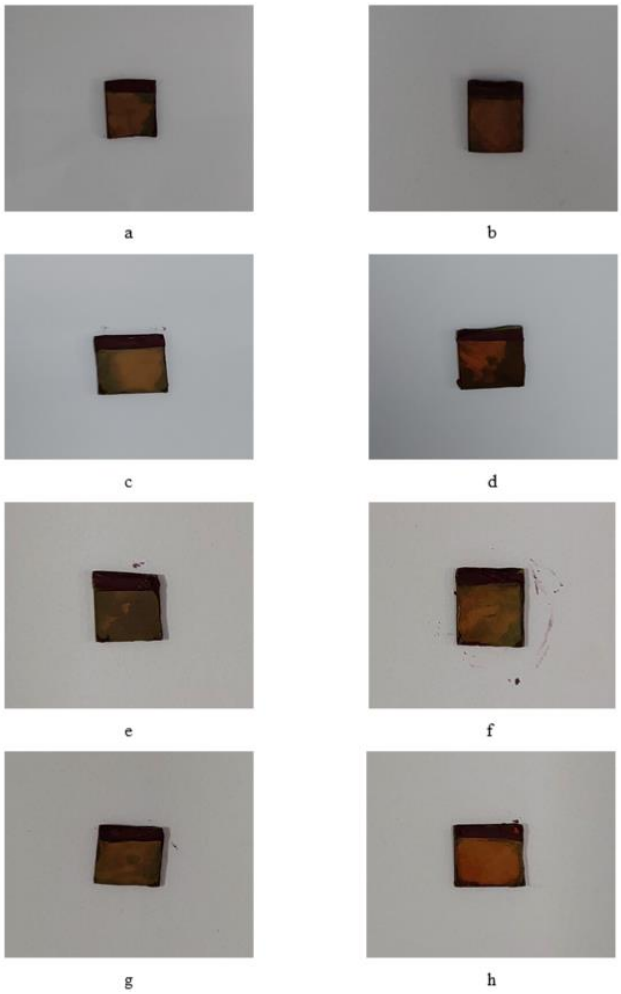

Figure 3.5. (a) undoped CdS and (b) 0.5% Mn, (c) 1% Mn, (d) 2% Mn, (e) 1% Co, (f) 3% Co, (g) 5% Co, (h) 7% Co doped CdS thin films coated with N719 and P3HT layers

The second solution was prepared by forming a mixture of 0.1 g P3HT, 0.05 g PCBM materials dissolved at 20 ml chlorobenzene. The solution was applied the same parameters with P3HT solution mentioned above and photographs of the coated samples of undoped, Mn-doped (0.5%, 1% and 2%) and Co-doped (1%, 3%, 5% and 7%) CdS thin films were shown in Figure 3.5, respectively.

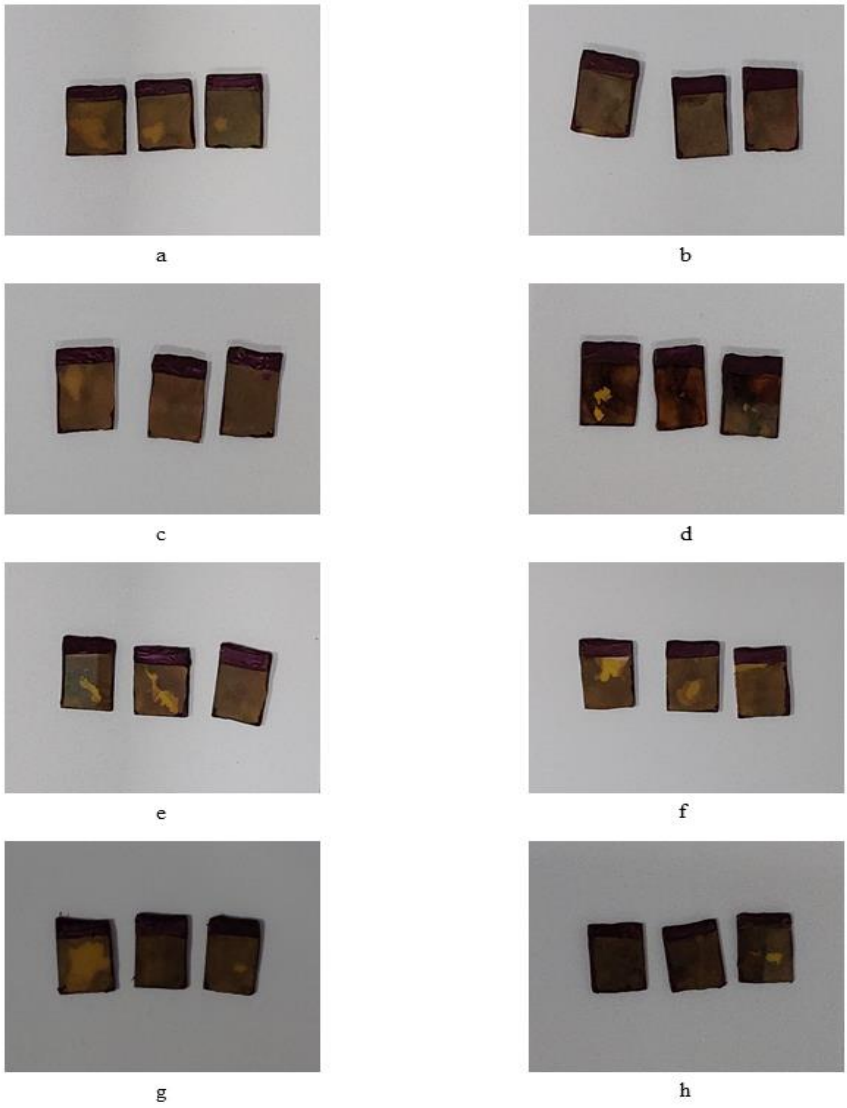

Figure 3.6. (a) undoped CdS and (b) 0.5% Mn, (c) 1% Mn, (d) 2% Mn, (e) 1% Co, (f) 3% Co, (g) 5% Co, (h) 7% Co doped CdS thin films coated with N719 and P3HT:PCBM layers.

3.6. Growth of PEDOT:PSS Layer by Spin Coating Method

PEDOT:PSS solution was prepared by 1:20 volume ratio with isopropyl alcohol. Then, solution was applied to the samples 20 times at 1 minute intervals at 100 rpm. The pictures of PEDOT:PSS coated samples of undoped, Mn-doped (0.5%, 1% and 2%) and Co-doped (1%, 3%, 5% and 7%) CdS thin films are shown in Figure 3.6, respectively.

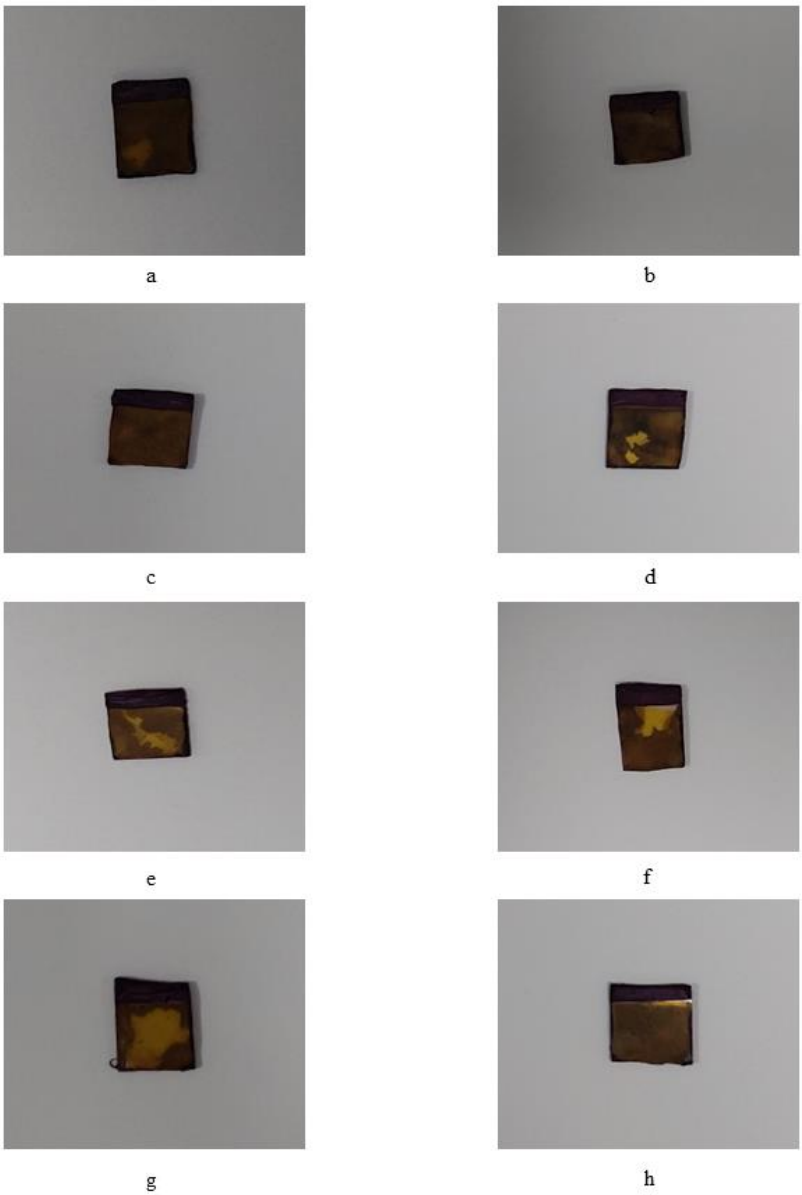

Figure 3.7. (a) undoped CdS and (b) 0.5% Mn, (c) 1% Mn, (d) 2% Mn, (e) 1% Co, (f) 3% Co, (g) 5% Co, (h) 7% Co doped CdS thin films coated with N719, P3HT:PCBM and PEDOT:PSS layer.

3.7. Fabrication of CdS-based Hybrid Solar Cells

Devices were finalized by applying a silver paste with a contact area of 0.008 cm^2 on top of all the produced layers. Names of the produced individual layer and the fabricated device structures are presented in Table 3.1.

Table 3.1. Codes of CdS-based samples with Co and Mn doping and their corresponding device configuration

Specimen's Code	Specimen's name
M0	ITO/CdS
M05	ITO/CdS:Mn (0.5 %)
M1	ITO/CdS:Mn (1 %)
M2	ITO/CdS:Mn (2 %)
M0-1	ITO/CdS/N719/P3HT
M05-1	ITO/CdS:Mn (0.5 %)/N719/P3HT
M1-1	ITO/CdS:Mn(1 %)/N719/P3HT
M2-1	ITO/CdS:Mn(2 %)/N719/P3HT
M0-2	ITO/CdS/N719/P3HT:PCBM
M05-2	ITO/CdS:Mn(0.5 %)/N719/P3HT:PCBM
M1-2	ITO/CdS:Mn(1 %)/N719/P3HT:PCBM
M2-2	ITO/CdS:Mn(2 %)/N719/P3HT:PCBM
M0-3	ITO/CdS:Mn(0 %)/N719/P3HT:PCBM/PEDOT:PSS
M05-3	ITO/CdS:Mn(0.5 %)/N719/P3HT:PCBM/PEDOT:PSS
M1-3	ITO/CdS:Mn(1 %)/N719/P3HT:PCBM/PEDOT:PSS
M2-3	ITO/CdS:Mn(2 %)/N719/P3HT:PCBM/PEDOT:PSS
C1	ITO/CdS:Co (1 %)
C3	ITO/CdS:Co (3 %)
C5	ITO/CdS:Co (5 %)
C7	ITO/CdS:Co (7 %)
C1-1	ITO/CdS:Co(1 %)/N719/P3HT
C3-1	ITO/CdS:Co(3 %)/N719/P3HT
C5-1	ITO/CdS:Co(5 %)/N719/P3HT
C7-1	ITO/CdS:Co(7 %)/N719/P3HT
C1-2	ITO/CdS:Co(1 %)/N719/P3HT:PCBM
C3-2	ITO/CdS:Co(3 %)/N719/P3HT:PCBM
C5-2	ITO/CdS:Co(5 %)/N719/P3HT:PCBM
C7-2	ITO/CdS:Co(7 %)/N719/P3HT:PCBM
C1-3	ITO/CdS:Co(1 %)/N719/P3HT:PCBM/PEDOT:PSS
C3-3	ITO/CdS:Co(3 %)/N719/P3HT:PCBM/PEDOT:PSS
C5-3	ITO/CdS:Co(5 %)/N719/P3HT:PCBM/PEDOT:PSS
C7-3	ITO/CdS:Co(7 %)/N719/P3HT:PCBM/PEDOT:PSS

3.8. Characterization of Produced Specimens and Fabricated Devices

The structural characterization of undoped, Mn-doped and Co-doped CdS specimens was carried out by X-ray diffraction measurement using CuKα radiation. XRD measurement was done in the interval of 20-60° with an increment step of 0.02°. Surface morphology of undoped, Mn-doped and Co-doped CdS layers and their devices were performed using scanning electron microscopy (SEM, JEOL JSM 6610). For analysing the elemental ingredients of undoped, Mn-doped and Co-doped CdS thin films, energy dispersive X-ray spectroscopy (EDS, Oxford Instruments) attached to SEM was used. Also, optical transmittance and absorption spectra of devices were measured with UV-Vis spectrophotometer (SpectraMax M5) between 300 nm and 1000 nm. For photoluminescence analyses of CdS-based thin films and their devices, Xenon flash lamb (Dongwoo Optron instrument) was used at an excitation wavelength of 280 nm operating at a power of 450 W. Current density-voltage (J-V) characteristics of undoped, Mn-doped and Co-doped CdS-based devices were determined through a source meter (Keithley 2410) at 100 mW/cm^2 power output under solar simulator (AM 1.5D illumination).

4. RESULTS AND DISCUSSION

In this section, a comprehensive analysis results of CdS thin films, individually doped with Mn and Co, and the corresponding solar cells fabricated on these thin films will be discussed.

4.1. XRD analysis of undoped, Mn and Co-doped CdS thin films

XRD plots of M0, M05, M1 and M2 samples are shown in Figure. 4.1. Specimens exhibit a polycrystalline structure, attributable to the reflection planes of (111), (220), and (311), corresponding to the cubic zincblende phase (JCPDS card no: 75-1546). M0 sample displays a preferred orientation along (111) plane. Notably, some peaks originating from ITO substrate are also visible in graphs. Examination of the patterns for M05, M1, and M2 specimens reveals that Mn-doping does not induce the formation of any new phase in CdS structure. This observation suggests successful introduction of Mn atoms into CdS host structure. Nevertheless, diminishing intensity of the (111) peak with increasing Mn-doping implies a decrease in crystal quality. Additionally, a pronounced reduction in peak intensities for (220) and (311) planes is evident with Mn-doping. Consistent with findings of Balpınar and co-authors, who reported analogous XRD patterns for Mn-doped CdS thin films, the present study confirms a Mn-induced decrease in intensities of (220) and (311) planes in CdS (Balpinar, 2020). Lattice parameter was calculated from the (111) plane using the equation below;

$$\frac{1}{d_{hkl}^2} = \frac{h^2+k^2+l^2}{a^2} \tag{4.1}$$

where d interplanar spacing, h, k, l are miller indices and a is the lattice constant.

For M0 specimen, lattice constant was found 0.579 nm. Upon Mn-doping, lattice parameters of CdS thin films exhibit an increase, reaching 0.582 nm for M2 specimen. It is expected that substitutional incorporation of Mn^{2+} ions into CdS host structure is irrational due to smaller ionic radius of Mn^{2+} ions (0.080 nm) compared to that of Cd^{2+} ions (0.097 nm). Consequently, the observed increment is likely attributed to interstitial incorporation of Mn atoms in CdS structure, leading to an expansion of unit cell volume of CdS sample.

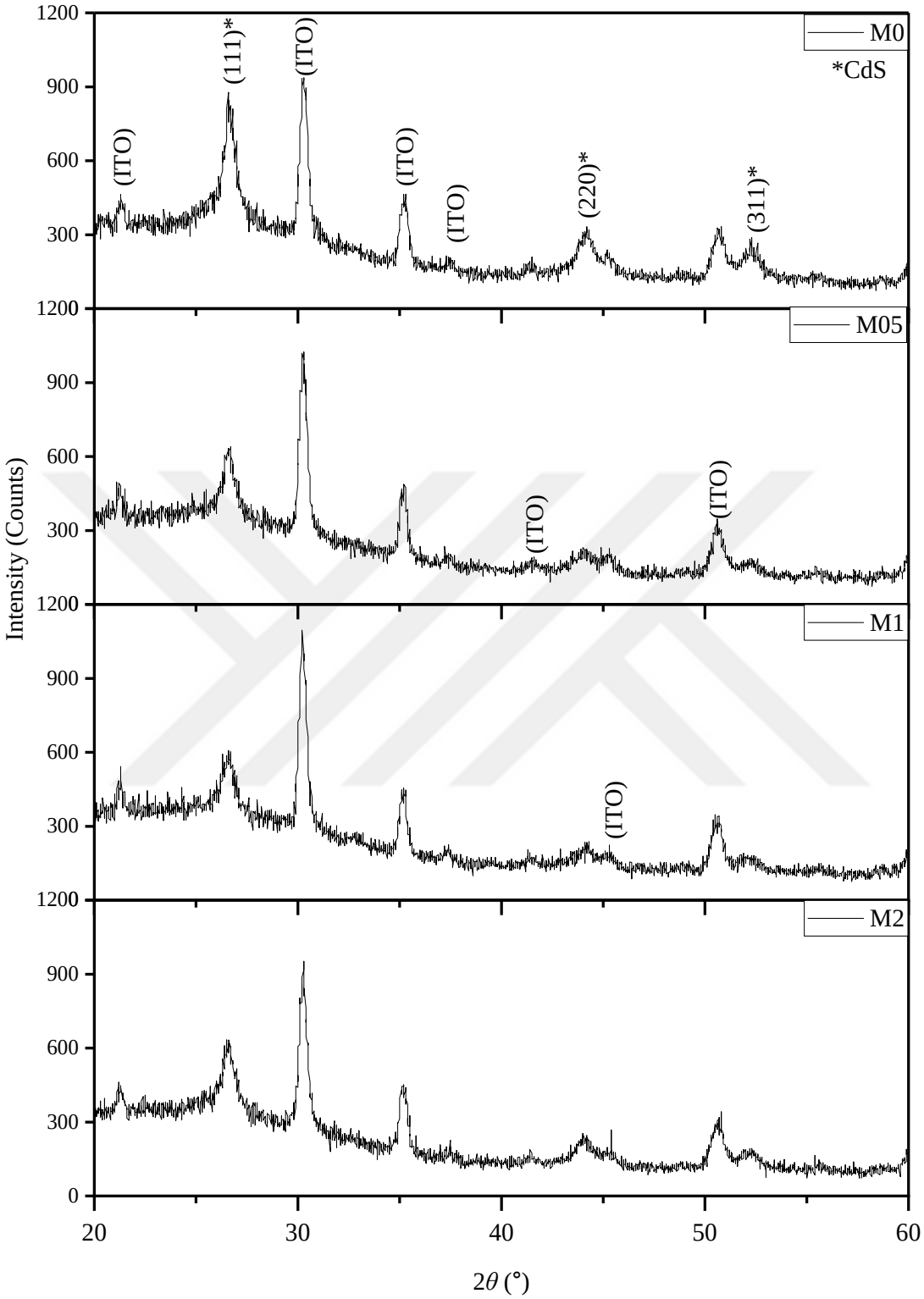

Figure 4.1. XRD graphs of Mn doped CdS thin films.

Crystalline size (D) is computed using Scherrer equation below;

$$D = \frac{0.94\lambda}{\beta \cos\theta} \tag{4.2}$$

where D is the crystalline size, λ is the wavelength of used X-ray, β is full width at half maximum (FWHM) in radians and θ is the Bragg diffraction angle. Calculation results are given in Table 4.1. M0 sample exhibits a crystalline size of 12.0 nm, which decreases to 10.7 nm with an increasing Mn-doping content of 2%. Reduction in D value is attributed to the hindering influence of Mn atoms on the growth process of CdS thin films. In agreement with Pitchaimani et al., who reported a decrease in crystalline size with increasing Mn-doping resulting from the substitutional incorporation of Mn^{2+} at Cd^{2+} ions in the CdS structure (Pitchaimani et al., 2016). Micro strain of samples is calculated by following formula;

$$\varepsilon = \frac{\beta \times \cos\theta}{4} \tag{4.3}$$

where ε is strain value, β is full-width at half-maximum.

Dislocation density (δ) is the number of dislocations per unit cell calculated by formula below;

$$\delta = \frac{1}{D^2} \tag{4.4}$$

where D is the crystallite size.

Table 4.1. presents micro-strain and dislocation density values, which exhibit an increase as Mn concentration rises from 0 to 2%. This increment is likely attributed to development of poor crystal quality after Mn doping.

Figure 4.2. illustrates XRD patterns of M0, C1, C3, C5, and C7 samples. Polycrystalline nature of M0 specimen is evident from peaks at 26.61°, 44.15°, and 52.31° corresponding to (111), (220), and (311) reflection planes of zinc blende cubic structure of CdS according to the JCPDS card no. 75-1546. Highest intensity is observed for the (111) peak, indicating a preferential

orientation along the (111) plane. However, relatively lower intensity of (111) plane suggests the presence of structural imperfections, leading to growth of sample with low crystal quality. Additional peaks detected in pattern arise from ITO-covered glass slides. In comparison to M0 sample, intensity of main (111) peak of CdS increases with increasing Co-doping until 5%, signifying an enhancement in crystal quality of CdS thin films. This finding aligns with the work of Kaur et al., who reported improved crystallinity in Co-doped CdS nanorods synthesized by solvothermal route (Kaur et al., 2013). Bairy et al. also observed a similar increase in intensity of (111) peak of CdS upon Co-doping for Co-doped CdS thin films synthesized by spray pyrolysis (Bairy et al., 2020). However, further dopings of Co at 5% and 7% lead to a remarkable decrease in the peak intensity of (111), indicating formation of CdS specimens with poor crystal quality due to introduction of more Co atoms in CdS structure, causing a distortion in the main matrix. This observation is consistent with previously reported works (Bacaksiz et al., 2008; Maity et al., 2019). Moreover, reduction in the intensity of (111) peak could be also attributed to a lower scattering factor for Co^{2+} ions compared to Cd^{2+} (Saravanan et al., 2011). It is noteworthy that Co-doping does not alter the crystallographic structure of CdS thin films, and the preferred orientation of CdS maintaines. No peaks associated with metallic Co or secondary phases, including CoO, CoS, CoS_2, and Co_3S_4, are observed within the detection limit of our device, confirming successful incorporation of Co atoms into CdS structure. As listed in Table 4.1, lattice constant (a) of M0 sample is 0.579 nm, and this value decreases to 0.576 for C7 sample. This reduction can be explained by substitutional incorporation of Co^{2+} ions at Cd^{2+} sites, as the ionic radius of Co^{2+} ions (0.074 nm) is lower than that of Cd^{2+} ions (0.097 nm), resulting in a reduction in unit cell volume of CdS. Crystalline size of specimens can be calculated using Scherrer's relation, and the results are tabulated in Table 4.1. M0 sample possesses a D of 12 nm, and this value fluctuates in the range of 13-15 nm, indicating no significant variation when Co atoms at different doping levels are introduced into CdS.

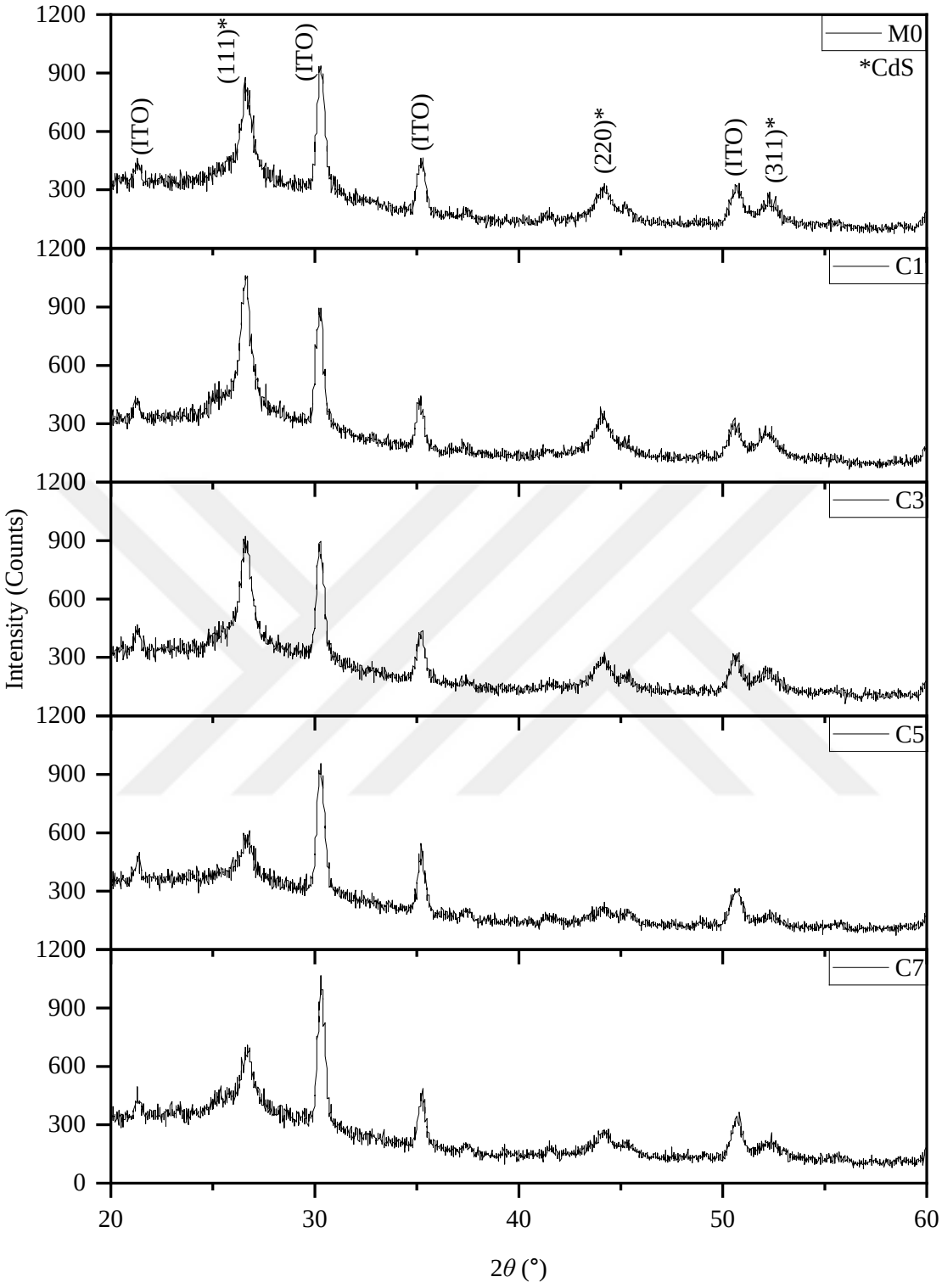

Figure 4.2. XRD graphs of Co doped CdS thin films

Table 4.1. Lattice constant, crystalline size, micro strain and dislocation density values of undoped and Mn and Co-doped CdS thin films

Specimen	Lattice costant (*a*) (nm)	Crystalline size (*D*) (nm)	Micro strain (**ε**) × (10^{-3})	Dislocation density × (10^{-3})
M0	0.579	12.0	2.89	6.94
M05	0.581	13.2	2.63	5.77
M1	0.581	11.5	3.01	7.57
M2	0.582	10.7	3.23	8.67
C1	0.579	14.8	2.33	4.53
C3	0.579	12.8	2.71	6.14
C5	0.580	11.5	3.01	7.56
C7	0.576	13.0	2.67	5.95

4.2. Morpholocigal analyses of undoped, Mn and Co-doped CdS thin films and their devices

Figure 4.3.(a)-(d) represent top-view images of samples labeled as M0, M05, M1, and M2 and all the data captured at the same magnification for precise comparison. It appears that M0 sample (Figure 4.3. (a)) reveals spherical grains uniformly covering the ITO surface with nearly identical mean sizes. These grains form through the agglomeration of small crystallites on surface, resulting in larger grains, alongside a relatively smooth surface topography dispersed with some voids. In contrast, upon the incorporation of 0.5% Mn atoms into CdS structure (Figure 4.3.(b)), M05 sample displays spherical-shaped grains but with a less uniform surface covering. Both small and large grains are discernible on the surface, yet there is no remarkable change in grain size compared to M0 sample. As for M1 sample (Figure 4.3.(c)), it shares similarities in grain shape with M05 sample in spite of exhibiting a smaller average grain size. Additionally, surface of M1 demonstrates a higher grain density than that observed in M05 sample. As for M2 specimen (Figure 4.3.(d)), it shows a smooth and uniform coating on ITO surface, preserving spherical grain shape. However, a noticeable reduction in mean grain size is evident in M2 sample, likely attributed to the reduced reaction rates upon Mn doping in CdS structure. It is acknowledged that smaller grain sizes arise from the slower formation of nucleation centers in thin films (Deka & Kalita, 2018). Researchers like Aksu et al. synthesized

Mn diffusion-doped CdS thin films through vacuum evaporation, noted an analogous reduction in grain size (Aksu et al., 2011). Similarly, Chaure conducted a wet chemical synthesis of Mn-doped CdS thin films, reporting a decrease in particle size from 7 nm to 5 nm with Mn atom incorporation (Chaure, 2019). Additionally, Figure 4.3.(e) illustrates a cross-section image of M2 specimen, revealing an approximate film thickness of 0.24 μm.

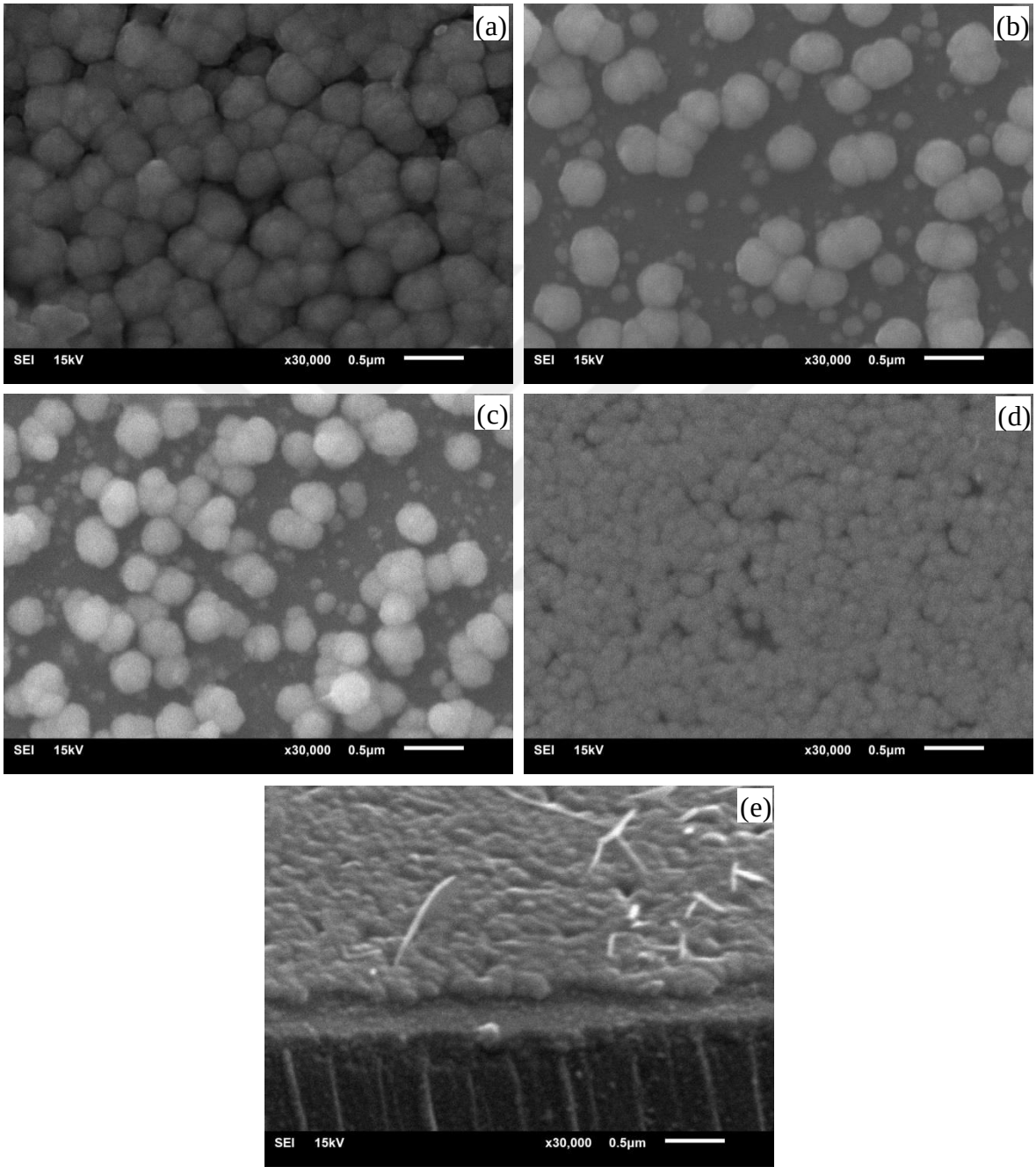

Figure 4.3. SEM plain view images of (a) M0, (b) M05, (c) M1, (d) M2 and (e) cross-section picture of M2 sample.

Figures 4.4.(a)-(e) present top-view images of samples labeled M0, C1, C3, C5, and C7, captured at identical magnifications for accurate comparative analysis. Figure 4.4.(a) reveals the picture of M0 sample displaying an underlying layer comprising small spherical grains on ITO-coated glass slides. Larger, round-shaped grains with average grain size of about 500 nm form atop on these smaller grains, possibly arising from the agglomeration of these smaller entities into larger CdS nanospheres. Presence of few voids between these nanospheres suggests a good density of spheres on surface. Upon Co-doping by 1% (Figure 4.4.(b)), diameter of CdS spheres reduces to approximately 250 nm. This significant reduction in sphere size may be attributed to altered reaction rates during Co incorporation into CdS, resulting in the slowed formation of nucleation centers in thin films, hence leading to a decrease in sphere size (Deka & Kalita, 2018). Correspondingly, Murugesan and co-workers andKumar et al. were reported similar conclusions regarding Co-doped CdS thin films upon Co-atom introduction into CdS structure (Kumar et al., 2014; Murugesan et al., 2019). Figures 4.4.(c) and (d) depict that surface morphologies of C3 and C5 samples remain largely unchanged compared to C1. However, C7 sample exhibits CdS nanospheres with the reduced sphere density on surface compared to other Co-doped CdS thin films. This reduction could be ascribed to degradation of CdS due to the increased incorporation of Co atoms into CdS host structure, consistent with XRD data. Furthermore, no pinholes or cracks are apparent on surfaces of any of specimens. Moreover, Figure 4.4.(f) provides data indicating that average thickness of C3 specimen is approximately 310 nm, indicating that less film thickness causes sufficient transparency suitable for solar cell applications.

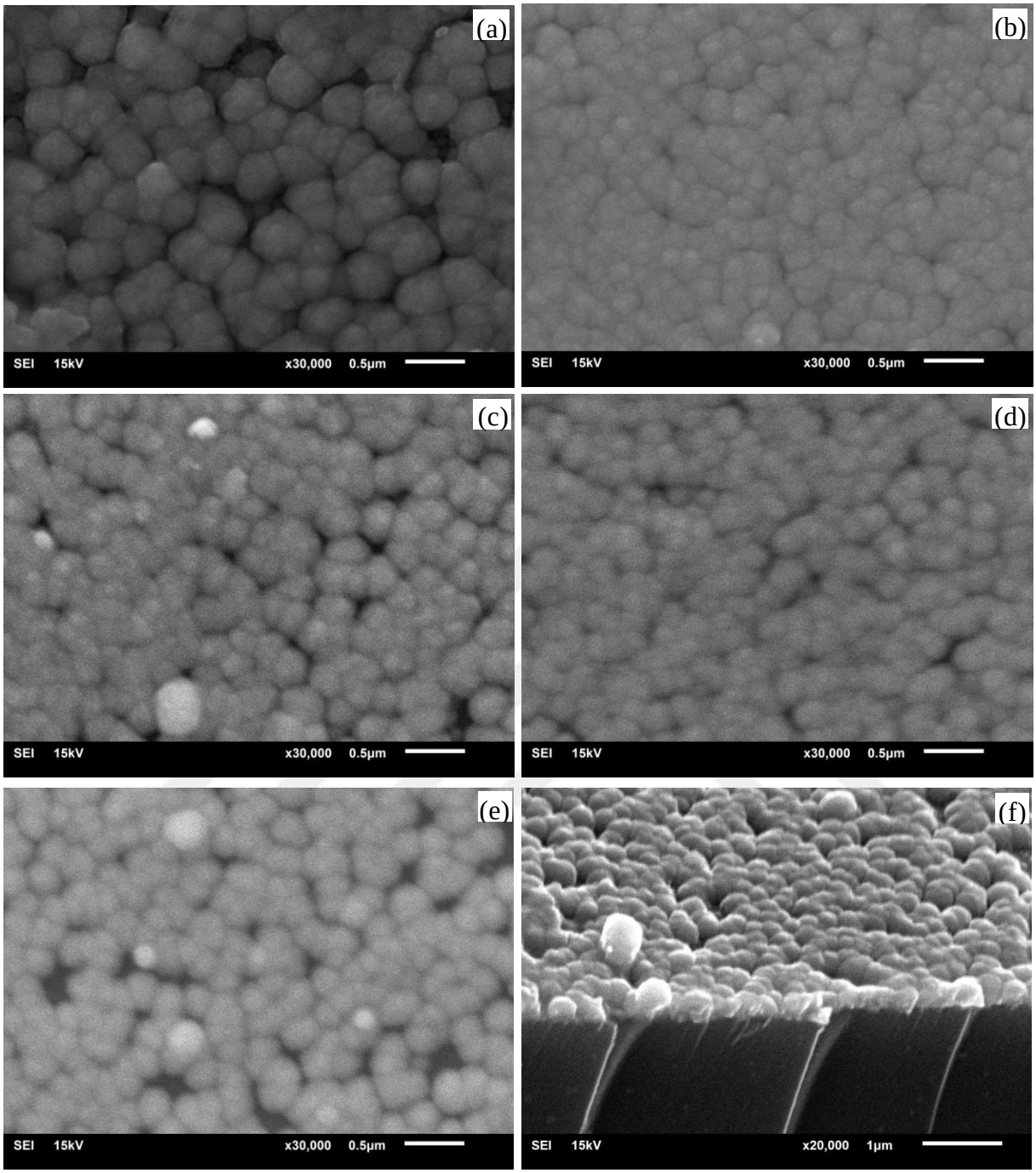

Figure 4.4. SEM photos of (a) M0, (b) C1 (c) C3, (d) C5, (e) C7 samples and a cross-section view of C3 sample.

SEM top-view images of devices labeled M0-3, M05-3, M1-3, and M2-3 are depicted in Figures 4.5.(a)-(d), respectively. Examination of SEM images for devices M0-3, M05-3, and M1-3 reveals an uneven distribution of P3HT:PCBM/PEDOT:PSS coating on the surfaces of M0, M05, and M1 samples. Notably, P3HT:PCBM/PEDOT:PSS layers exhibit covering primarily on spherical grains of both CdS and Mn-doped CdS thin films. These coated grains are

interlinked through a web-like structure. However, the cover of P3HT:PCBM/PEDOT:PSS on M2 sample presents a distinctive contrast. In this case, a uniform and smooth coating of P3HT:PCBM/PEDOT:PSS is observed without any formation of voids or cracks on surface, suggesting the achievement of a thin layer coating for M2-3 device. Furthermore, Figure 4.5.(e) provides a cross-sectional view of M2-3 device, revealing a measured thickness of approximately 0.34 μm. Consequently, thickness of P3HT:PCBM/PEDOT:PSS layers is estimated to be approximately 0.10 μm.

Figures 4.6.(a)-(e) exhibit top-view images of devices labeled M0-3, C1-3, C3-3, C5-3, and C7-3, respectively. Upon examination, it becomes evident that P3HT:PCBM/PEDOT:PSS layers do not uniformly cover surfaces of M0, C5, and C7 samples. There is an absence of a continuous film cover on these samples, with P3HT:PCBM/PEDOT:PSS bilayer primarily coating the spherical grains of these samples. Additionally, a web-like appearance of P3HT:PCBM/PEDOT:PSS is observed on the surface of M0 specimen. In contrast, C1-3 and C3-3 devices present a distinct coating pattern. Here, P3HT:PCBM/PEDOT:PSS bilayer covers uniformly and smoothly surfaces of C1 and C3 samples, resulting in formation of a continuous thin layer. Notably, there are no observed cracks, voids, or clusters on the surfaces of these samples, affirming a well-applied surface coating of P3HT:PCBM/PEDOT:PSS for C1-3 and C3-3 devices. Furthermore, Figure 4.6.(f) provides a cross-sectional view of C3-3 device, indicating a total thickness of approximately 0.50 μm. Consequently, estimated thickness of P3HT:PCBM/PEDOT:PSS bilayer is approximately 0.19 μm.

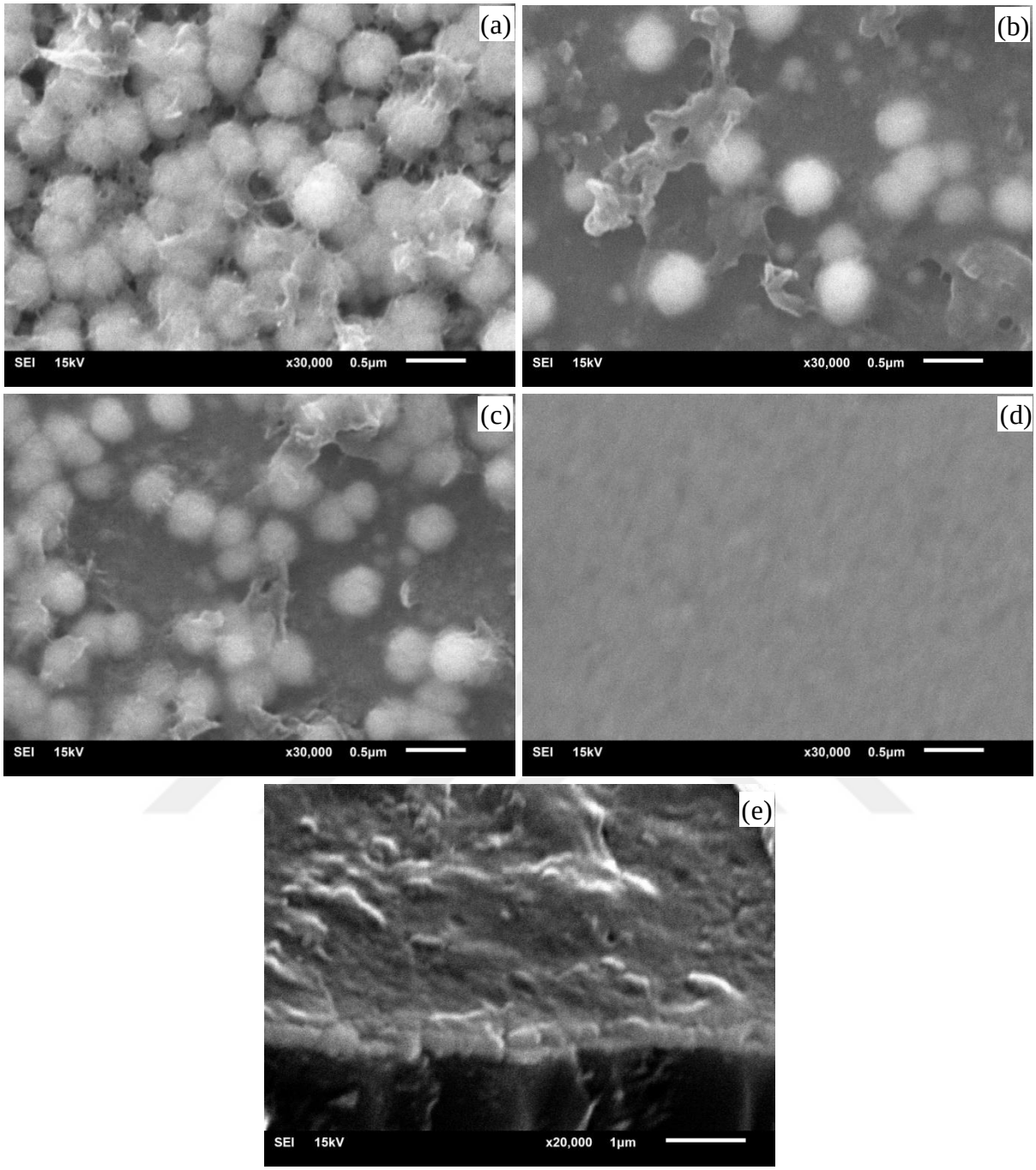

Figure 4.5. SEM plain view images of (a) M0-3, (b) M05-3, (c) M1-3, (d) M2-3 devices and cross-section picture of M2-3 devices.

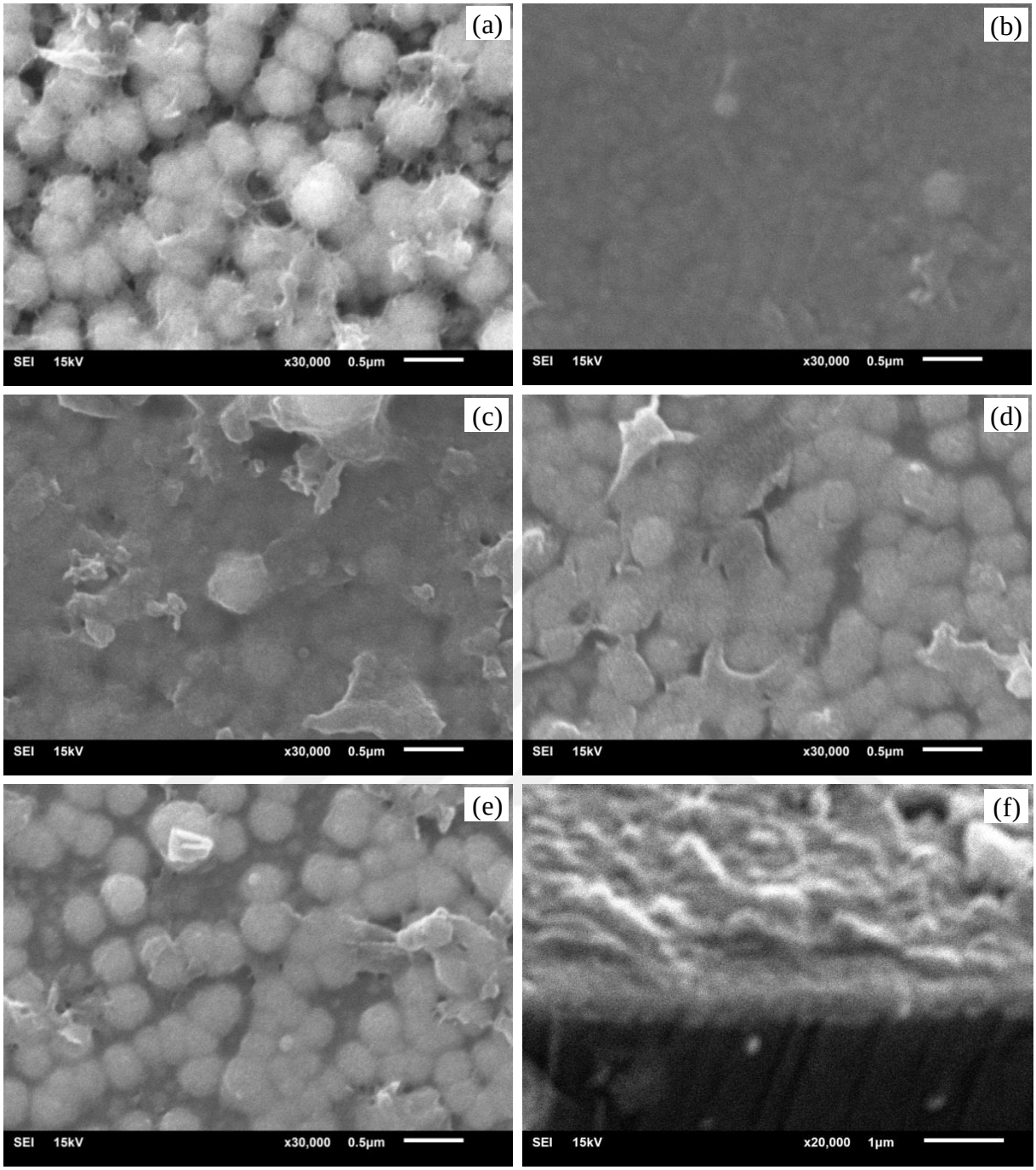

Figure 4.6. SEM plain view photos of (a) M0-3, (b) C1-3, (c) C3-3, (d) C5-3, (e) C7-3 devices and (f) a cross section view of C3-3 device.

4.3. Elemental composition analyses of undoped, Mn and Co-doped CdS thin films

Figures 4.7.(a)-(d) display EDS survey spectra of samples labeled M0, M05, M1, and M2, respectively. These spectra reveal the presence of Cd, S, and Mn elements in both undoped and Mn-doped CdS thin films, without any indication of other impurities. Notably, it's observed that nominal concentrations of Mn doping are higher than actual concentrations. This discrepancy could potentially stem from non-uniform distribution of Mn atoms within CdS structure. Furthermore, Mn doping introduces variations in the atomic concentration of CdS structure. Specifically, Cd/S ratio differs among the samples. In M0 sample, this ratio is calculated to be 1.04, whereas it increases to 1.08 for M05 sample. However, for M1 and M2 samples, this ratio decreases to 1.03 and 0.93, respectively. This observation suggests that Mn doping leads to the formation of a non-stoichiometric CdS structure.

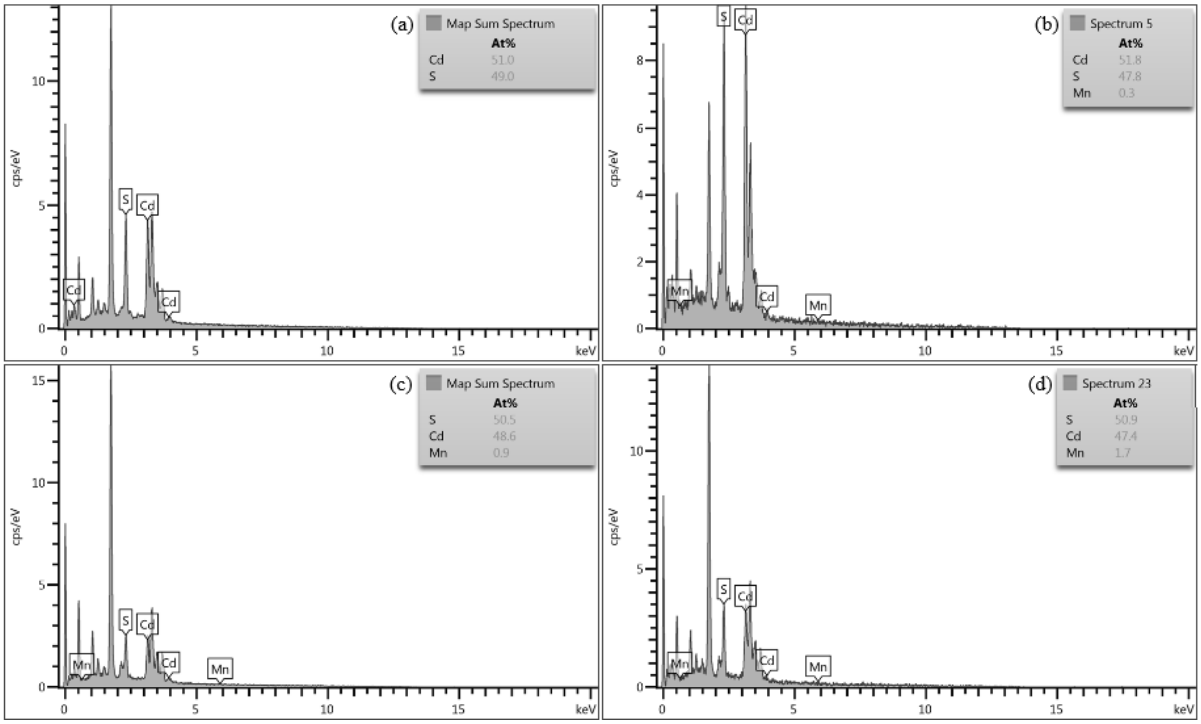

Figure 4.7. EDS survey spectra of M0, M05, M1 and M2 samples.

Figures 4.8.(a)-(e) present EDS spectra of samples labeled M0, C1, C3, C5, and C7, respectively. Analysis reveals that M0 sample solely contains Cd and S elements, whereas Co elements are detected in addition to Cd and S in C1, C3, C5, and C7 samples without any presence of other impurity atoms. Notably, actual atomic concentrations of Co in CdS are found to be lower than nominal concentrations, potentially due to non-uniform distribution of Co

atoms within CdS structure. Moreover, it's observed that actual atomic density of Co atoms in CdS increases with higher levels of Co doping. Calculation of Cd/S ratio provides further insights as follows: M0 sample displays a Cd/S ratio of 1.04. However, this ratio decreases to 1.01 for C1 and C3 samples, indicating formation of stoichiometric CdS growth. Conversely, this ratio increases to 1.03 for C5 specimen and reaches its highest value of 1.06 for C7 sample. This trend confirms that a higher concentration of Co doping leads to development of non-stoichiometric CdS thin films.

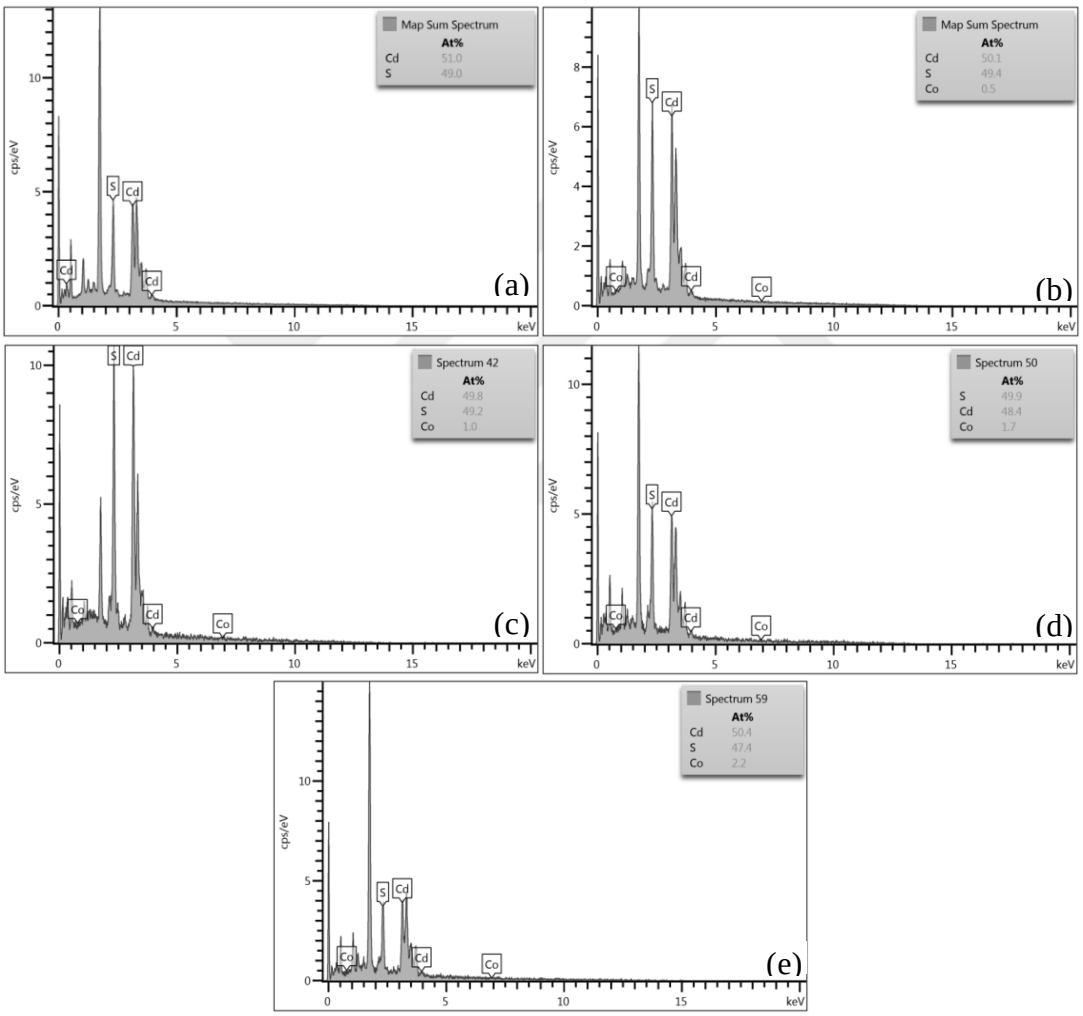

Figure 4.8. EDS survey spectra of (a) M0, (b) C1 (c) C3, (d) C5 and (e) C7 samples.

4.4. Optical Analyses of undoped, Mn and Co-doped CdS thin films and devices

Figure 4.9. displays transmittance plots of specimens labeled M0, M05, M1, and M2. M0 sample shows a transmission of 5% within the 300 nm-500 nm range, followed by an upward trend as wavelength boosts from 500 nm to 1000 nm, reaching a peak of 55% at 1000 nm. This

low transmission might be attributed to light scattering at the grain boundaries. Notably, M05 sample exhibits increased transmission between 300 nm and 500 nm without altering the curve's shape. Bilgin and co-workers reported a similar conclusion for Mn-doped CdO thin films with incorporation of Mn in CdO structure (Bilgin et al., 2006). Similarly, M1 sample demonstrates comparable data, except for its intensity within the 300 - 500 nm range. However, a distinct characteristic is observed in M2 sample. It displays an upward trend starting from 300 nm, reaching a maximum transparency exceeding 90% between 500 nm and 650 nm. Subsequently, transmittance value declines between 650 nm and 900 nm, stabilizing at 70% at 1000 nm. This notable increase in transmission in CdS thin films upon 2% Mn doping is likely due to the formation of a smoother surface, as indicated in SEM data, which decays light scattering, resulting in higher transparency (Demirselcuk et al., 2021). It's known that CdS samples with higher transmittance are favorable for solar cell applications.

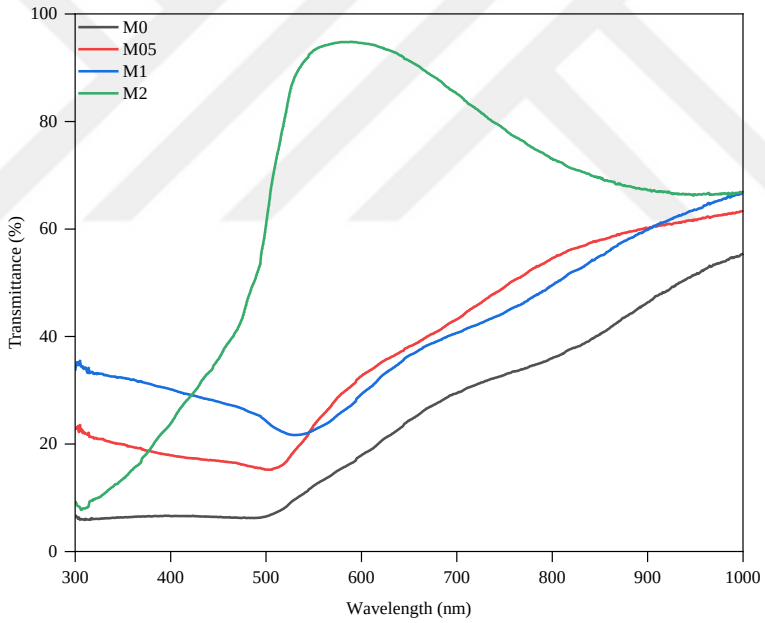

Figure 4.9. Transmittance plots of undoped Mn doped CdS films.

Figures 4.10. presents transmittance graphs of C-series samples and Figure 4.11. demonstrates P3HT:PCBM blend, respectively. Figure 4.10. illustrates that M0 specimen displays a 5% transmittance within the 300 to 500 nm range, steadily increasing to a maximum of 55% at 1000 nm. This lower transparency might be attributed to light scattering at grain boundaries. In contrast, C1 specimen exhibits approximately 85% transparency in visible and near-infrared regions, highest among all Co-doped CdS samples. Well-defined interference fringes in

transmittance likely result from a smooth surface and good sample homogeneity observed in Figure 4.4. As for C3 sample, it shows an increasing trend as wavelength varies from 500 nm to 1000 nm, reaching the highest transmission of nearly 70% at 850 nm. Compared to M0 sample, substantial increase in transmissions of C1 and C3 specimens may be due to the enhanced crystal quality discussed in XRD data. Similarly, C5 sample demonstrates a curve akin to C3 sample in spite of a different transparency value. C3 sample achieves maximum transparency of 65% at 1000 nm. Conversely, C7 specimen shows an ascending trend up to 750 nm and then declines toward 1000 nm, reaching around 80% maximum transparency at 750 nm. A research by Shaban et al. noted that 8% Co-doped CdS samples exhibited highest transmission, whereas lower Co doping resulted in the reduced transparency compared to undoped CdS (Shaban et al., 2020). In this study, all Co-doped CdS thin films show higher transparency than undoped counterpart, suggesting the improved optical effects of Co atoms in CdS structure. However, a slight reduction in transparency of C5 specimen might be attributed to a degradation in crystal quality. Nevertheless, development of more transparent CdS films after 7% Co doping could be related to the reduced dislocation density, resulting in lower light scattering and variations in sample thickness. In summary, Co doping enhances transparency of CdS thin films that is an fundamental characteristic for solar cell applications. Additionally, Figure 4.11. demonstrates the transmission data of the P3HT:PCBM blend, revealing an increase in absorption edge between 550-650 nm, followed by a linear rise in transmittance up to 1000 nm, reaching almost 99% transparency, indicating material's exceptional transparency.

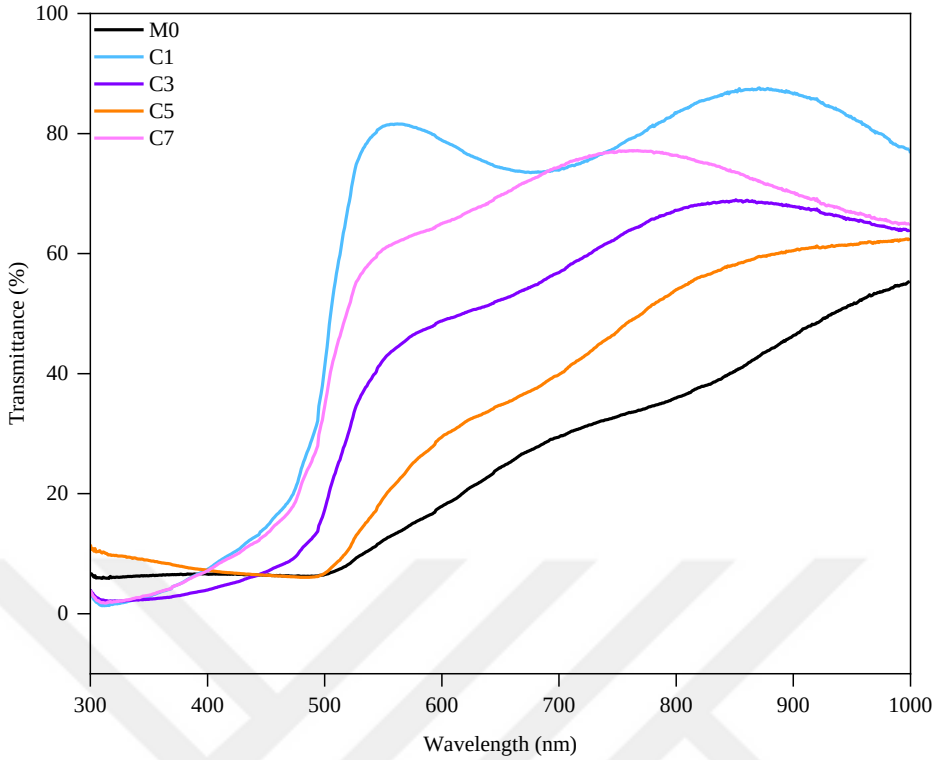

Figure 4.10. Transmittance curves of undoped and Co doped CdS thin films.

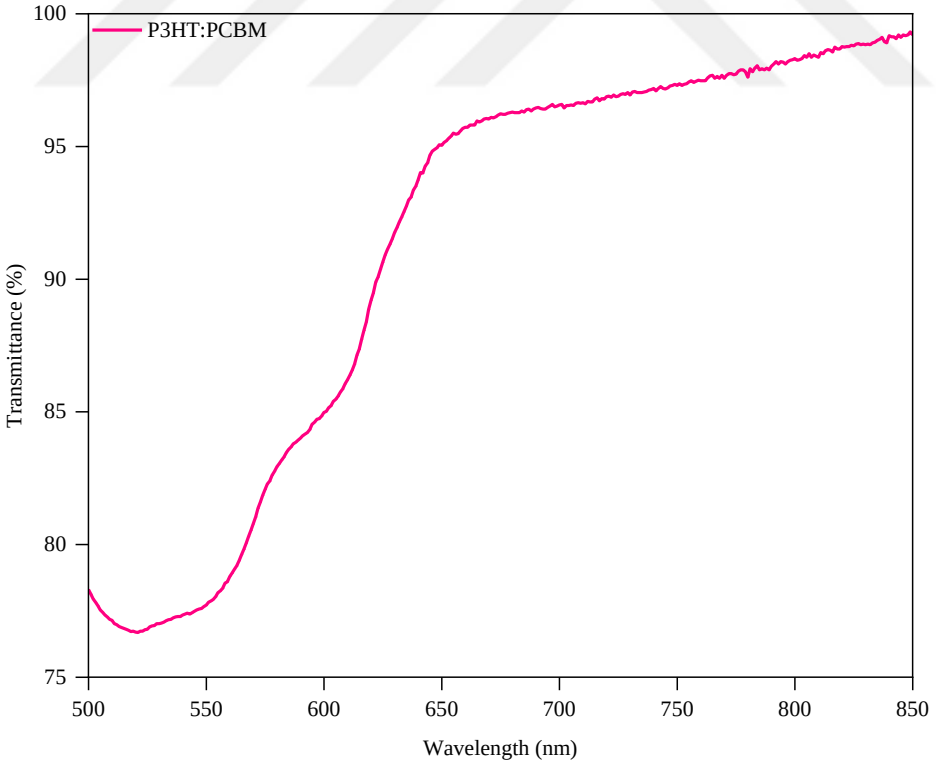

Figure 4.11. Transmittance data of P3HT:PCBM organic layer.

Absorption edges for samples of M0, M05, and M1 display a relatively soft transition, whereas M2 sample exhibits an obvious and sharp increase in the absorption edge, suggesting better crystal quality in this sample. Band gaps for these samples were calculated using Tauc's extrapolation method and results data are graphed in Figure 4.12. Additionally, band gap values for all specimens are tabulated in Table 4.2. M0 sample shows a band gap of 2.10 eV, slightly lower than band gap of bulk CdS material (2.42 eV at 300 K), which aligns well with band gap values reported for chemically bath-deposited CdS samples (El-Shaer et al., 2023; Kathirvel et al., 2011; Ruiz-Ortega et al., 2023). Band gap of M05 sample decreases to 2.05 eV, and a more substantial reduction is observed in M1 sample, which records a band gap of 1.84 eV. This reduction is attributed to sp-d exchange interactions between localized d electrons of Mn^{2+} ions and band electrons of CdS (Aksu et al., 2011; Girish et al., 2021). Additionally, an increase in defect states due to Mn doping might also contribute to this decline (Girish et al., 2021). Conversely, band gap value for M2 sample remarkably increases to 2.94 eV, surpassing that of M0 sample. There exists an inverse relationship between crystal size and band gap, known as the quantum confinement effect. As discussed in XRD results, M2 sample demonstrates smallest crystalline size, resulting in an enlarged band gap for this specimen. Another factor contributing to this increase could be ascribed to the band bowing induced by chemical disorder following an increased amount of Mn^{2+} ions in CdS structure, affirming findings in previous literature (Chuu et al., 1997; Devi et al., 2014). In summary, M2 sample appears to be the most suitable material for solar cell applications due to its enlarged band gap.

In Figure 4.12., a distinct increase in the absorption edge implies energy band gap with sharper edges, indicating higher crystal quality. Accordingly, C1 sample appears to exhibit the most notable crystal quality due to sharpness of its absorption edge. Band gaps for M0, C1, C3, C5, C7, and P3HT:PCBM samples are determined using Tauc's approximation method and are visualized in Figure 4.12. and Figure 4.13, respectively while also tabulated in Table 4.2. M0 sample demonstrates a band gap of 2.10 eV, slightly lower than that of bulk CdS. This finding aligns with prior reports on CdS samples grown via CBD route (El-Shaer et al., 2023; Kathirvel et al., 2011; Ruiz-Ortega et al., 2023). Comparatively, band gap for C1 sample increases to 2.43 eV, consistent with previous studies (Contreras-Rascón et al., 2018; Pitchaimani et al., 2016; Tomakin et al., 2014). However, band gap decreases to 2.34 eV for C3 specimen and further to 2.22 eV for C5 sample. This decline could be attributed to sp-d exchange interactions between valence band electrons of CdS and localized d electrons of Co^{2+}, and possibly increasing lattice

strain. In contrast, C7 sample exhibits a larger band gap of 2.40 eV compared to C3 and C5, potentially due to the development of non-stoichiometric CdS thin films as discussed in EDS results. Thus, it can be inferred that C2 specimen is the most suitable material for solar cells among the tested samples. Band gap analysis of P3HT:PCBM blend films shown in Figure 4.12. reveals two band gaps at 1.96 eV and 2.06 eV. The first band gap is associated with P3HT, as its known band gap falls within the range of 1.9 – 2.0 eV. Additionally, chosen molar ratio of P3HT:PCBM as 2:1 predominantly influences P3HT in the blend films, resulting in the appearance of P3HT's band gap according to the Tauc's analysis. Moreover, the reported works suggested that PCBM easily diffused into P3HT, creating crystalline and amorphous regions within P3HT when blended with PCBM. Therefore, the second band gap in P3HT:PCBM blend films is attributed to the P3HT:PCBM structure, contributing to an enlargement in the band gap of P3HT due to formation of this blend structure (Korte et al., 2023; McLeod et al., 2015; Xie et al., 2020).

Table 4.2. Forbidden band gap values of undoped, Mn doped and Co doped CdS thin films

Specimen Code	Band gap (eV)
M0	2.10
M05	2.05
M1	1.84
M2	2.94
C1	2.43
C3	2.34
C5	2.22
C7	2.40

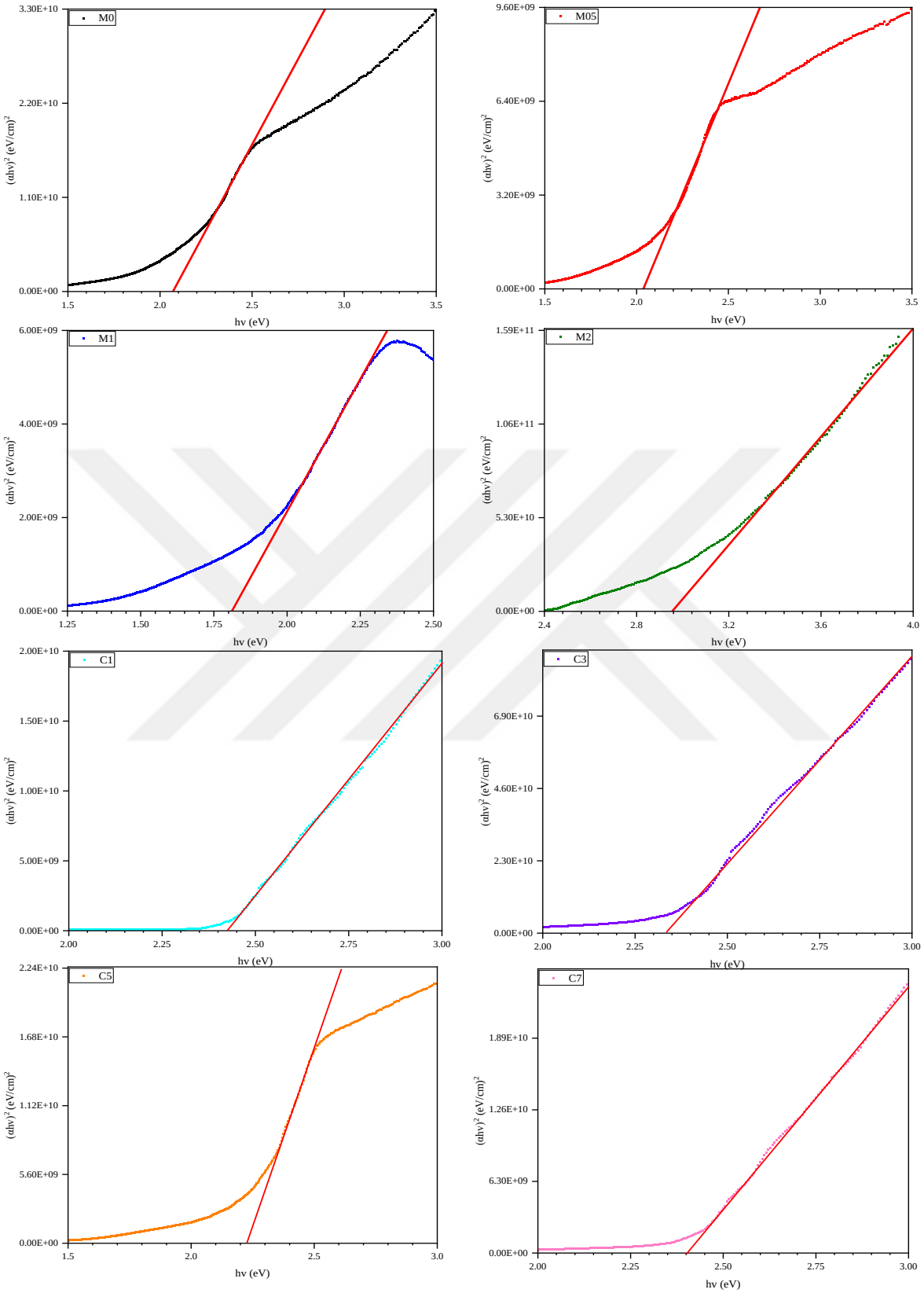

Figure 4.12. Tauc plots of undoped, Mn and Co-doped CdS thin films.

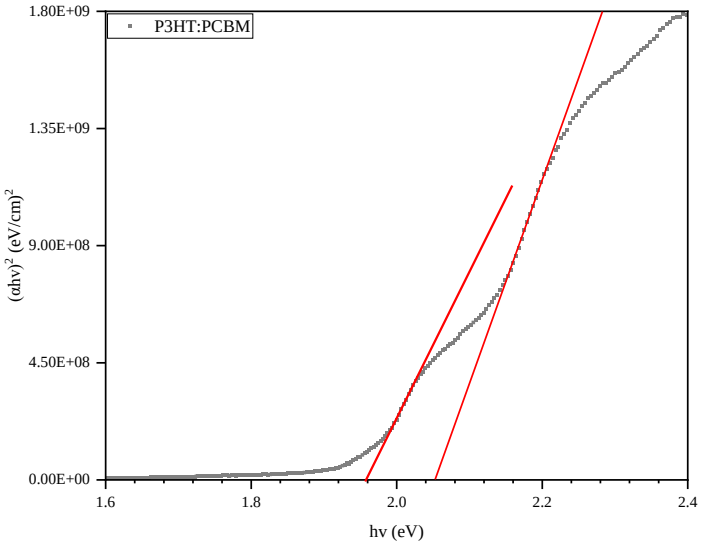

Figure 4.13. Tauc plot of P3HT:PCBM blend organic thin film.

Figure 4.14. presents absorbance plots for M0, M05, M1, and M2 specimens. M0 sample displays a broad absorbance spectrum with an onset of absorption at 484 nm. Both M05 and M1 samples exhibit absorption spectra similar to M0 although their intensities are notably lower than that of M0. Additionally, the absorption edges for M05 and M1 occur at 505 nm and 530 nm, respectively. However, the most distinctive absorbance behavior is observed in M2 sample. This specimen displays an absorption onset at 589 nm with the lowest intensity among the samples. Moreover, compared to the M0 sample, the absorption edge of M2 specimen is blue-shifted. This shift is attributed to the quantum size effect resulting from a reduction in crystalline size due to an increased amount of Mn ions in CdS. These observations align with findings reported in previous studies (Gadalla et al., 2018; Ganguly & Nath, 2020; Gupta & Kripal, 2012).

In Figure 4.15., absorption curves of M0, C1, C3, C5, and C7 samples are illustrated. M0 sample maintains consistent absorption within the 300-500 nm range, followed by a decline attributed to the emergence of interband transitions as wavelength increases. Conversely, C1 sample exhibits a distinct pattern with a peak at 310 nm, followed by a decrease in absorption between 340-450 nm, and an absorption onset at 539 nm. Moreover, a broad peak is observed between 600 and 800 nm, likely due to tetrahedral coordination of Co^{2+} ions in CdS (Muruganandam et al., 2015). Absorption curves of C3 and C7 samples resemble the curve of C1 sample in terms of their curve characteristic despite variations in intensities and absorption onsets. Specifically,

absorption onsets for C3 and C7 specimens are measured at 571 nm and 546 nm, respectively. Comparatively, all Co-doped CdS thin films show reduced intensities in the 500-1000 nm wavelength range compared to M0 sample. This reduction in absorbance could be attributed to lattice structure defect states resulting from differences in the ionic radii of Cd^{2+} and Co^{2+} ions, as well as light scattering due to grain boundaries. Pitchaimani et al. investigated Co and Mn-doped CdS thin films, examining their structural, optical, and antibacterial properties, and found that Co-doping led to a reduction in absorbance of CdS thin films (Pitchaimani et al., 2016). Additionally, the absorbance curve of C5 sample closely resembles absorption behavior of M0 specimen, particularly in shorter wavelength region. C5 specimen exhibits the decreased absorption below a wavelength of 430 nm. Notably, there is an observed blue-shift in the fundamental absorption edge of CdS thin films due to the incorporation of Co atoms, indicating an enlargement in the band gap.

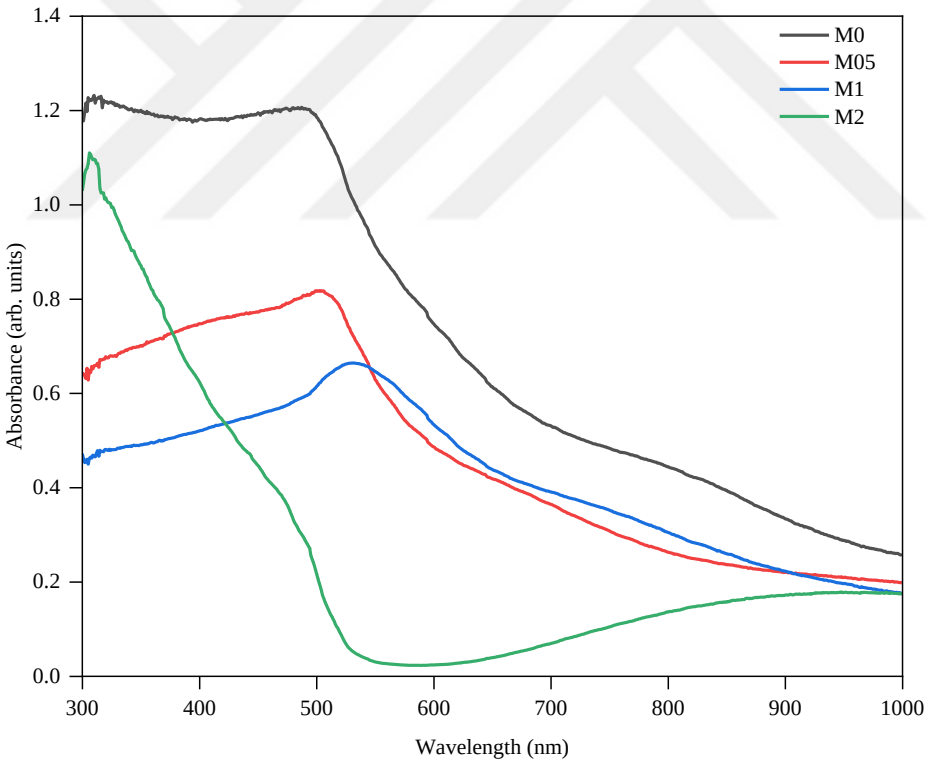

Figure 4.14. Absorbances of undoped and Mn doped CdS films

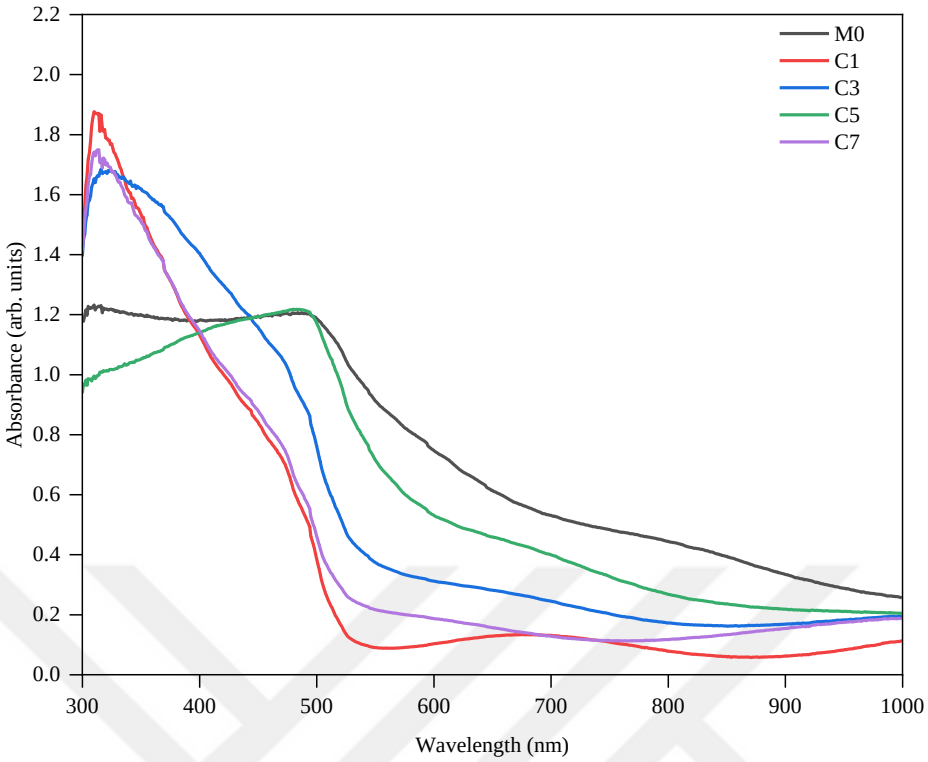

Figure 4.15. Absorbances of undoped and Co doped CdS films

Figure 4.16. displays RTPL (room temperature photoluminescence) plots of M0, M05, M1, and M2 samples. It's well known that emissions in CdS stem from point defects like sulfur vacancies (V_S), sulfur interstitials (I_S), cadmium vacancies (V_{Cd}), and cadmium interstitials (I_{Cd}). M0 sample demonstrates four prominent peaks in its spectrum located at 421 nm, 482 nm, 535 nm, and 647 nm. First peak relates to band-edge emission originating from electron-hole pair recombination, consistent with earlier work (Mercy et al., 2014). Second peak corresponds to the host CdS structure (Yılmaz et al., 2017), third ascribes to V_S in CdS (Ahmed et al., 2017), and last at 647 nm imputes to V_{Cd} due to surface defects (Yılmaz, Tomakin, et al., 2020). M05, M1, and M2 samples exhibit similar curve characteristics to M0, with no significant changes in peak positions upon Mn atoms incorporation in CdS. However, M05 sample shows the highest peak intensity compared to M0, possibly due to the introduction of a small amount of Mn atoms in CdS, acting as luminescent centers and enhancing radial recombination rates, thus intensifying the peaks. Previous research conducted by Jadhav et al. supported this, indicating an increase in PL peak intensity with Mn-doping (Jadhav et al., 2017). Interestingly, M1 sample shows no notable change in PL intensity for moderate Mn-doping. However, M2 exhibits the lowest PL intensity among all CdS thin films. This decline could be attributed to the higher amount of incorporation of Mn atoms, potentially leading to non-radiative recombination

processes (Barglik-Chory et al., 2003). Similar conclusions were obtained by other researchers studying Mn-doped CdS nanostructures (Barglik-Chory et al., 2003; Ji et al., 2011). Another reason for the decrease in PL peak intensity might be recombination between V_{Cd} and I_{Cd} defects, causing a loss of these defects in CdS structure and subsequently reducing PL intensity. EDS evidence supports this claim, indicating more V_{Cd} defects in CdS structure of M2 compared to M0.

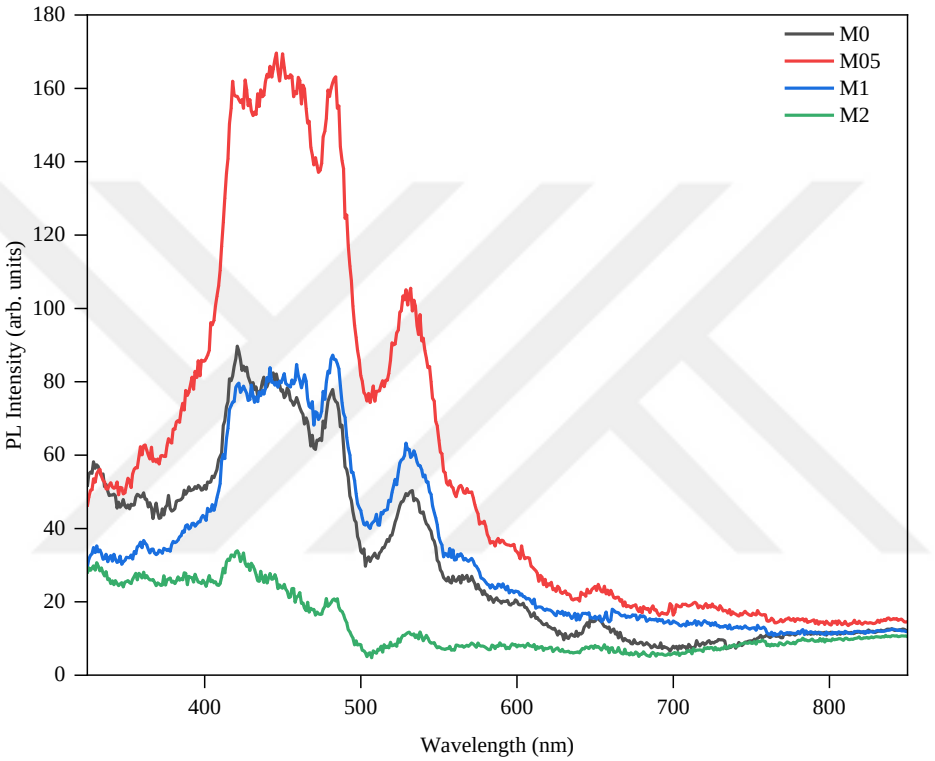

Figure 4.16. RTPL data of undoped and Mn doped CdS films

Figure 4.17. represents RTPL curves of P3HT, P3HT:PCBM, M0-2, M05-2, M1-2, and M2-2 heterostructures to examine the quenching effect caused by the P3HT:PCBM blend. The conventional PL curve of P3HT falls between 550 nm and 800 nm and dominates the PL spectra of M0-2, M05-2, and M1-2 samples. However, the P3HT:PCBM blend exhibits a low PL peak intensity due to the presence of PCBM, leading to a significant quenching resulting from electron transfer from photo-excited P3HT to PCBM (Huang et al., 2013). Interestingly, M0-2, M05-2, and M1-2 heterostructures display higher peak intensities compared to P3HT:PCBM blend, suggesting less successful exciton dissociation at the CdS:Mn/P3HT:PCBM interface. Conversely, efficient exciton dissociation occurs between CdS and P3HT:PCBM layers as evidenced by the lower PL peak intensity of M2-2 heterostructure compared to P3HT:PCBM.

Similar quenching effects in PL peak intensity were reported by Jabeen et al. for Mn-doped CdS quantum dots-based solar cells and by Yılmaz et al. for Ni-doped CdS-based hybrid solar cells (Jabeen et al., 2018; Yılmaz, Tomakin, et al., 2020). Enhanced exciton dissociation at the interface typically leads to the improved device performance. In summary, considering all observations of CdS thin films with and without Mn-doping, it can be concluded that 2% Mn-doped CdS thin films exhibit the most optimized structural, morphological, and optical properties, making them a promising candidate for use in CdS-based hybrid solar cells.

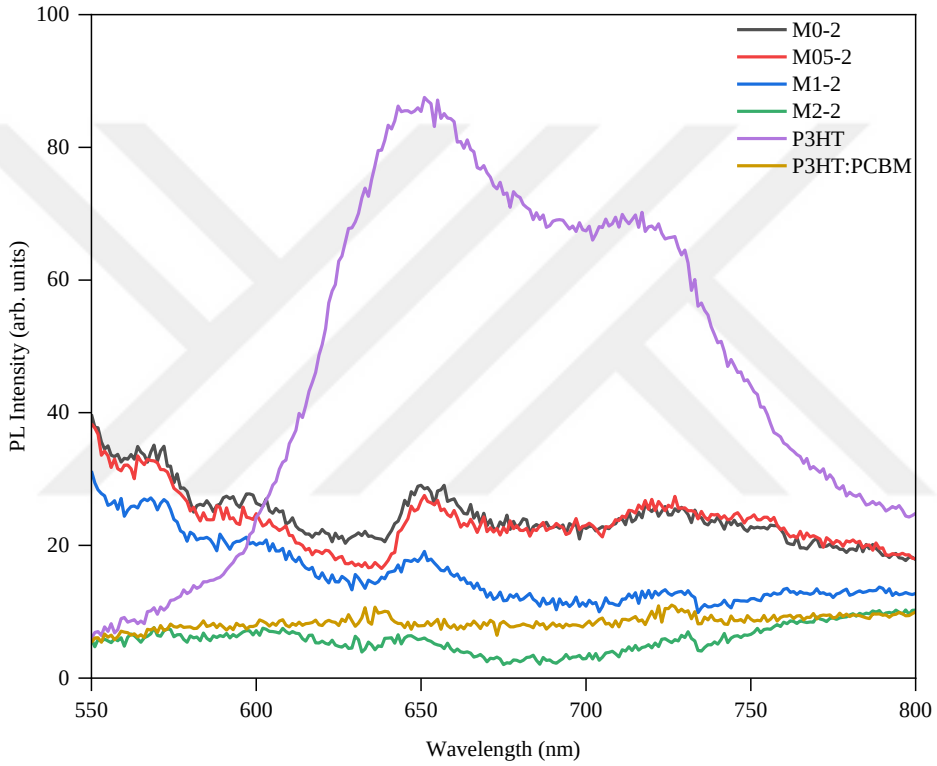

Figure 4.17. RTPL curves of M0-2, M05-2, M1-2, M2-2 devices and P3HT, P3HT:PCBM layers

Figure 4.18. displays photoluminescence (PL) spectra of M0, C1, C3, C5, and C7 specimens, highlighting the intrinsic defects present in CdS thin films such as V_S, I_S, V_{Cd}, and I_{Cd}. M0 sample exhibits four prominent peaks at 421 nm, 482 nm, 535 nm, and 647 nm. First peak corresponds to near-band-edge emission attributed to electron-hole recombination (Mercy et al., 2014). Second peak is related to CdS host structure, while the third is linked to V_S defects in CdS (Ahmed et al., 2017; Yılmaz et al., 2017). Fourth peak likely indicates V_{Cd} induced by surface defects (Yılmaz, Tomakin, et al., 2020). All samples display similar PL emission behavior although they vary in intensity. Notably, the introduction of Co atoms in CdS structure

does not alter the peak positions of CdS sample. M0 specimen shows highest PL peak intensities for the first and last peaks, whereas C5 exhibits maximum intensities for the second and third peaks. However, compared to M0, PL peak intensities of C1, C3, and C7 samples decrease, proposing a reduction in defects within the thin films. Furthermore, decrease in PL peak intensity suggests the development of non-radiative recombination processes due to the creation of additional defect states, which act as non-radiative recombination centers. This reduction might also be explained by recombination occurring between I_{Cd} and V_{Cd} defects, leading to a decrease in the number of these defects. A similar quenching effect upon Co-doping in CdS was reported by Ibraheem et al. for Co-doped CdS quantum dots (Ibraheem et al., 2020).

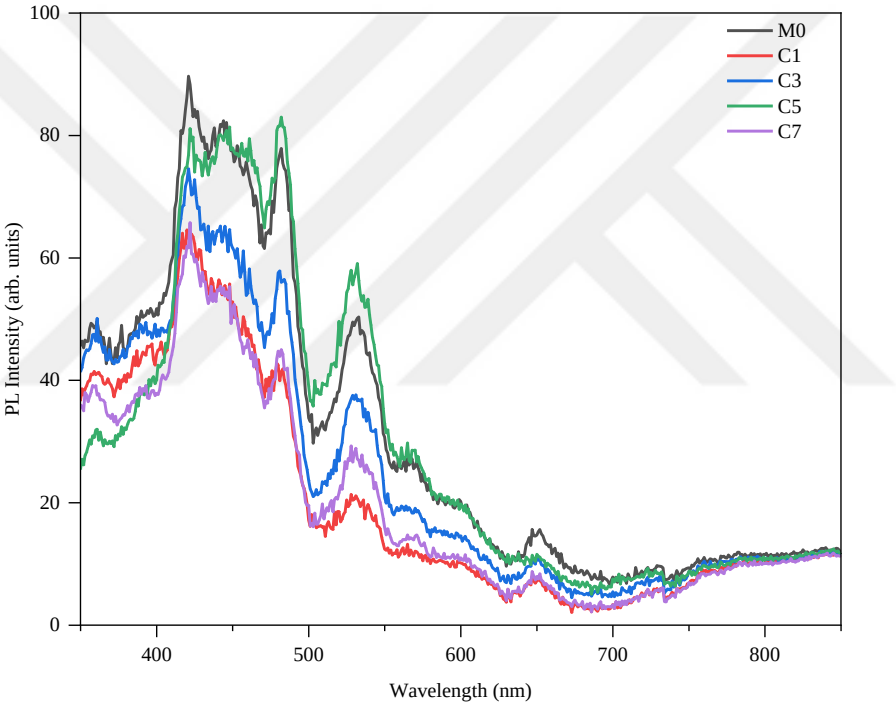

Figure 4.18. RTPL data of undoped and Co doped CdS films

In summary, the inclusion of Co atoms in CdS thin films leads to an enhancement in their structural, morphological, and optical properties. Among the studied samples, C1 stands out with its superior structural, morphological, and optical characteristics over the others. These findings indicate that C1 sample possesses optimized data, implying its potential utilization in hybrid solar cell applications.

4.5. Photovoltaic performance of devices

J-V curves of M0-3 and M2-3 devices are indicated in Figure 4.19., along with the photovoltaic parameters listed in Table 4.3. Notably, both M0-3 and M2-3 devices exhibit distinct photovoltaic characteristics. M0-3 device demonstrates a J_{SC} of 1.517 mA.cm^{-2}, V_{OC} of 0.158 V, FF of 0.265, and a PCE of 0.070%. However, the attained PCE value is relatively low due to a decreased fill factor, which could be attributed to the higher surface roughness reported for chemical bath deposited CdS thin films, affecting fill factor adversely (Wright & Uddin, 2012). In contrast, M2-3 device exhibits significantly improved photovoltaic performance with a J_{SC} of 5.677 mA.cm^{-2}, V_{OC} of 0.124 V, FF of 0.259, and an overall efficiency of 0.202%. Notably, J_{SC} value of M2-3 device is approximately four times higher than that of M0-3 device. This substantial increase in J_{SC} is attributed to the incorporation of Mn atoms in CdS, which facilitates efficient charge transfer at the interface by reducing charge recombination rate through formation of mid-gap states within band gap. Enhanced PCE value observed in M2-3 device can be attributed to several factors: (i) SEM analysis indicates that M2 sample possesses improved surface smoothness compared to M0, which is essential for better contact formation between P3HT:PCBM and CdS:Mn layers in solar cell applications. (ii) as depicted in Figure 4.9., M2 specimen exhibits notably higher transmittance compared to M0, enabling more efficient light transmission into the interface to form more excitons (iii) substantial quenching of PL peak observed for P3HT:PCBM blend concerning M2-2 specimen signifies successful exciton dissociation at the interface, contributing to enhanced device performance (iv) as discussed in Figure 4.16., lower PL peak intensity of M2 sample across the spectrum implies development of a less intrinsically defected CdS sample, leading to an improved PCE (v) M2 sample displays a higher band gap (2.94 eV) compared to M0 (2.10 eV) and a decrease in crystallite size upon 2% Mn-doping, causing a shift in conduction band of CdS, which aligns well with the LUMO state of the P3HT:PCBM active layer, a phenomenon consistent with previous studies. Researches made by Ganguly et al. on Mn-doped CdS quantum dots and done by Li et al. on CdS quantum dots sensitized solar cells through Mn-doping were also observed efficiency improvements, affirming the substantial impact of Mn-doping on enhancing the efficiency of CdS-based hybrid solar cells (Ganguly & Nath, 2020; Li et al., 2014).

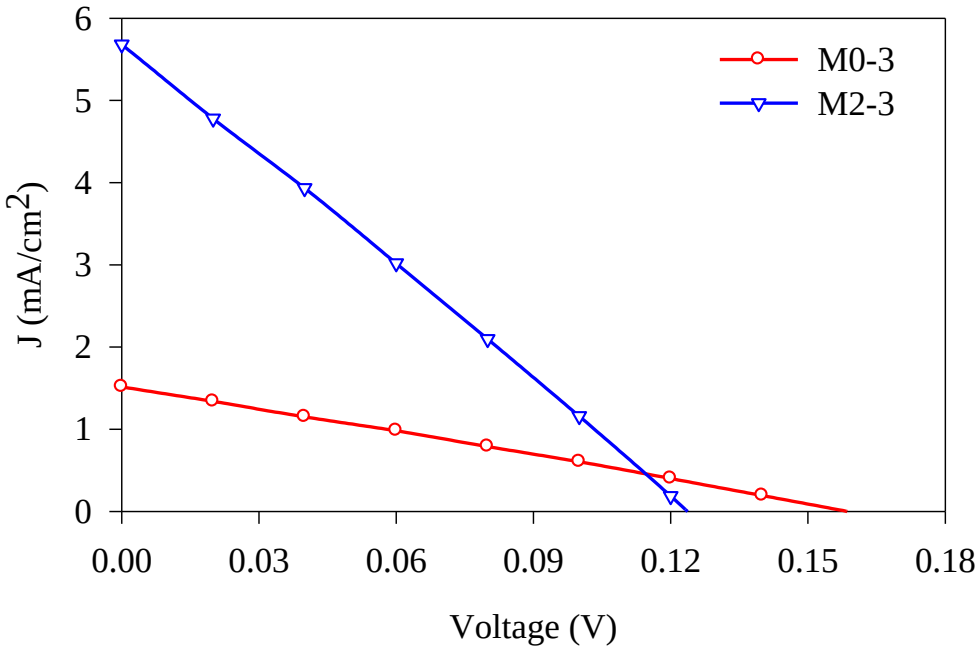

Figure 4.19. J-V curves of M0-3 and M2-3 devices

J-V characteristics of M0-3, C1-3, C3-3, C5-3, and C7-3 devices are depicted in Figure 4.20, and the corresponding photovoltaic parameters are presented in Table 4.3. It's evident that all hybrid solar cells exhibit distinct photovoltaic behavior. M0-3 device displays a J_{SC} of 1.517 mA.cm^{-2}, V_{OC} of 0.158 V, and an overall efficiency of 0.070%, which is relatively low due to a low fill factor. This reduced fill factor might be attributed to greater surface roughness, as seen in similar studies with CdS thin films grown by CBD route (Wright & Uddin, 2012). However, C1-3 device demonstrates notably improved photovoltaic parameters, with a J_{SC} of 7.014 mA.cm^{-2}, V_{OC} of 0.221 V, FF of 0.285, and PCE of 0.488%. Efficiency enhancement in the solar cell upon 1% Co-doping mainly stems from increased J_{SC} value. This boost in J_{SC} is attributed to the creation of mid-gap states within the forbidden band gap due to the incorporation of a low amount of Co atoms in CdS structure, facilitating efficient charge transfer at interface and reducing charge recombination. Several factors contribute to the improved efficiency of C1-3 device: (i) enhanced surface morphology observed in SEM data (Figure 4.4.(b)) for C1 sample, leading to a better interface between CdS:Co and P3HT:PCBM layers, which is advantageous for solar cells (ii) highest transparency exhibited by C1 sample (Figure 4.10.), allowing efficient light transmission, thus creating more excitons at the interface (iii) lower PL peak intensity observed for C1 sample (Figure 4.18.), indication of a less defected CdS structure, contributing to the improved efficiency (iv) higher band gap of C1 sample compared to M0, resulting in a shift in conduction band of CdS, aligning better with LUMO

state of P3HT:PCBM. A study realized by Firoozi et al. on Co-doped CdS nanoparticles for quantum dots sensitized solar cells also showed an enhancement in PCE values with increased Co ion concentration in CdS (Firoozi et al., 2015). However, the efficiency of C3-3 device deteriorates compared to C1-3, and further Co-doping to 5% and 7% (C5-3 and C7-3) results in lowest PCE values for CdS-based devices. This decline in PCE values for higher Co-doping concentrations is likely due to crystal quality degradation in CdS samples, variation in sample transparency, and reduced exciton dissociation between CdS and P3HT:PCBM layers. Therefore, both Co-doping and its atomic concentration in CdS are crucial factors in achieving efficient CdS-based hybrid solar cells.

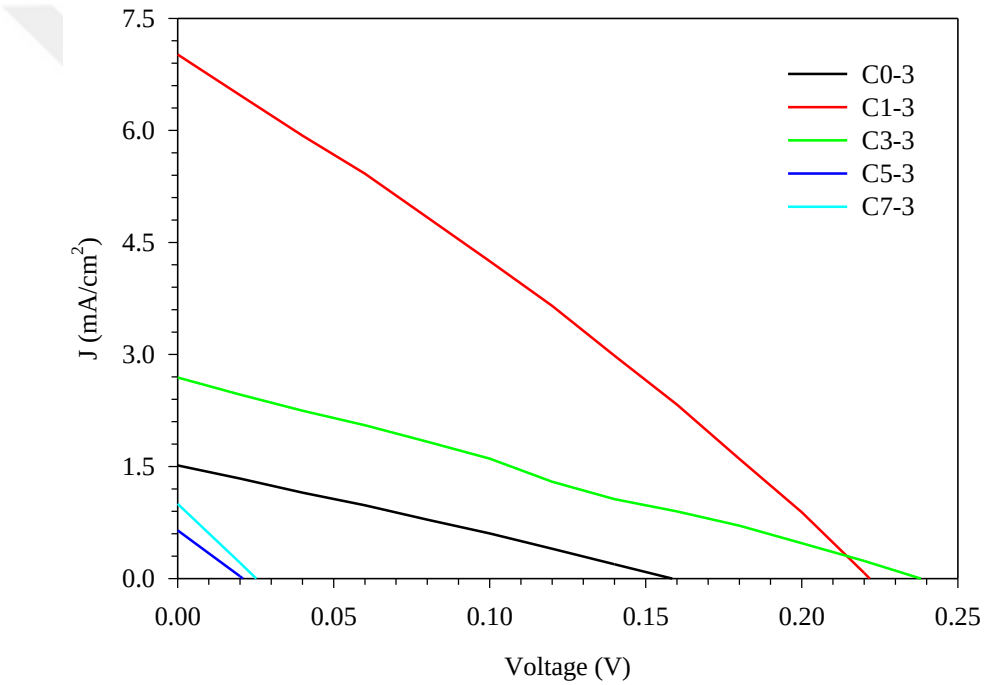

Figure 4.20. J-V plots of C0-3, C1-3, C3-3, C5-3, C7-3

Table 4.3. J-V characteristics of M0-3, M2-3, C1-3, C3-3, C5-3, C7-3 devices.

Device	J_{SC} **(mA.cm^{-2})**	V_{OC} **(V)**	***FF***	*Ƞ (%)*
M0-3	1.517	0.158	0.265	0.070
M2-3	5.677	0.124	0.259	0.202
C1-3	7.014	0.221	0.283	0.488
C3-3	2.696	0.238	0.251	0.179
C5-3	0.643	0.021	0.202	0.003
C7-3	1.000	0.025	0.218	0.006

5. CONCLUSION

Synthesis of CdS thin films using chemical bath deposition led to production of both undoped and Mn-doped CdS films on ITO-coated glass substrates. XRD analysis highlighted that the introduction of Mn atoms in CdS structure increased dislocation density and micro-strain, indicating a decline in crystal quality. SEM imaging confirmed that while M0 and M2 samples had uniform and smooth surfaces, M05 and M1 specimens exhibited poor coatings. Additionally, size of CdS grains notably reduced for M2 samples. Presence of Mn in CdS films was validated through EDS. Analysis of transmittance data revealed that Mn-doping positively affected transparency of CdS films, notably observed in M2 samples with over 90% transparency in the 500–650 nm wavelength range. Mn incorporation caused band gap of CdS to increase from 2.10 eV to 2.94 eV, resulting in a blue shift in absorption edge due to the quantum confinement effect. PL characteristics showed a variation in intensity among Mn-doped CdS films, with M05 having the highest PL intensity and M2 with the lowest. Furthermore, PL spectrum of M2-2 indicated more efficient exciton dissociation at Mn:CdS/P3HT:PCBM interface. J-V measurements highlighted that while M0-3 device had an efficiency of 0.070%, highest PCE of 0.202% was achieved for M2-3 device, emphasizing the beneficial effect of Mn incorporation in CdS-based hybrid solar cells.

Furthermore, Co-doped CdS thin films were also prepared via CBD method and hybrid solar cells utilizing these films were fabricated. XRD analysis revealed a cubic structure with a preferential orientation along the (111) plane for all samples. Co-doping induced a decrease in unit cell volume of CdS by substituting Co^{2+} ions at Cd^{2+} sites. SEM observations demonstrated a reduction in CdS grain size by approximately 250 nm upon Co-doping, potentially due to slower nucleation center formation in thin films. Optical transmission was significantly improved for Co-doped CdS films, reaching up to 85% in visible region due to the enhanced crystal quality. Co-doping initially increased the band gap of CdS films to 2.43 eV for C1 sample, but Co concentration led to a decrease in the band gap to 2.22 eV for C5 sample due to sp-d exchange interaction. After Co-doping, absorbance above 500 nm decreased, attributed to light scattering at grain boundary. PL intensity reduced for Co-doped CdS films due to additional defect states induced by Co-doping. Notably, while C1-3 device achieved a champion PCE of 0.488% due to an increase in J_{SC}, further Co-doping resulted in a significant decline in the overall efficiency of CdS-based hybrid solar cells.

REFERENCES

Ahmed, B., Ojha, A. K., & Kumar, S. (2017). One-pot synthesis of Ni doped CdS nanosheets for near infrared emission and excellent photocatalytic materials for degradation of MB dye under UV and sunlight irradiation. *Spectrochimica Acta - Part A: Molecular and Biomolecular Spectroscopy*, *179*, 144–154. https://doi.org/10.1016/j.saa.2017.02.007

Aksay, S., Polat, M., Özer, T., Köse, S., & Gürbüz, G. (2011). Investigations on structural, vibrational, morphological and optical properties of CdS and CdS/Co films by ultrasonic spray pyrolysis. *Applied Surface Science*, *257*(23), 10072–10077. https://doi.org/10.1016/j.apsusc.2011.06.142

Aksu, S., Bacaksiz, E., Parlak, M., Yilmaz, S., Polat, I., Altunba, M., Türksoy, M., Topkaya, R., & Özdoan, K. (2011). Structural, optical and magnetic properties of Mn diffusion-doped CdS thin films prepared by vacuum evaporation. *Materials Chemistry and Physics*, *130*(1–2), 340–345. https://doi.org/10.1016/j.matchemphys.2011.06.046

Bacaksiz, E., Tomakin, M., Altunbaş, M., Parlak, M., & Çolakoğlu, T. (2008). Structural, optical and magnetic properties of Cd1-xCo xS thin films prepared by spray pyrolysis. *Physica B: Condensed Matter*, *403*(19–20), 3740–3745. https://doi.org/10.1016/j.physb.2008.07.006

Bairy, R., Kulkarni, S. D., Murari, M. S., & Narasimhamurthy, K. N. (2020). An investigation of third-order nonlinear optical and limiting properties of spray pyrolysis-deposited Co:CdS nanostructures for optoelectronics. *Applied Physics A: Materials Science and Processing*, *126*(5). https://doi.org/10.1007/s00339-020-03549-8

Balpinar, N. (2020). FABRICATION AND CHARACTERIZATION OF DYE-SENSITIZED SOLAR CELLS BASED ON MUREXID DYE AND INORGANIC CdS:Mn THIN FILMS. In *Chalcogenide Letters* (Vol. 17, Issue 9).

Barglik-Chory, C., Remenyi, C., Dem, C., Schmitt, M., Kiefer, W., Gould, C., Rüster, C., Schmidt, G., Hofmann, D. M., Pfisterer, D., & Müller, G. (2003). Synthesis and characterization of manganese-doped CdS nanoparticles. *Physical Chemistry Chemical Physics*, *5*(8), 1639–1643. https://doi.org/10.1039/b300343d

Bilgin, V., Akyuz, I., Kose, S., & Atay, F. (2006). Characterization of Mn-incorporated CdO films grown by ultrasonic spray pyrolysis. *Semiconductor Science and Technology*, *21*(5), 579–585. https://doi.org/10.1088/0268-1242/21/5/001

Chandrasekaran, J., Nithyaprakash, D., Ajjan, K. B., Maruthamuthu, S., Manoharan, D., & Kumar, S. (2011). Hybrid solar cell based on blending of organic and inorganic materials - An overview. In *Renewable and Sustainable Energy Reviews* (Vol. 15, Issue 2, pp. 1228–1238). Elsevier Ltd. https://doi.org/10.1016/j.rser.2010.09.017

Chaure, S. (2019). Investigation of the effect of Manganese doping in CdS nanocrystalline thin films. *Materials Research Express*, *6*(2). https://doi.org/10.1088/2053-1591/aad4e1

Chen, H. Y., Kao, S. H., & Lin, C. F. (2013). Review on Recent Progress on Sandwich-Structure Hybrid Solar Cells. *Energy Technology*, *1*(7), 382–391. https://doi.org/10.1002/ente.201300044

Chuu " ', D.-S., Chang, Y.-C., & Hsieh, C.-Y. (1997). th 2_n Growth of CdMnS films by pulsed laser evaporation. In *Thin Solid Films* (Vol. 304).

Contreras-Rascón, J. I., Díaz-Reyes, J., Linares-Avilés, M. E., Rivera-Hernández, K. N., Galván-Arellano, M., Arias-Cerón, J. S., & Martínez-Juárez, J. (2018). Characterization of CBD–CdS nanocrystals doped with Co2+. *Journal of Materials Science: Materials in Electronics*, *29*(23), 19748–19756. https://doi.org/10.1007/s10854-018-0100-3

Cortina, H., Martínez-Alonso, C., Castillo-Ortega, M., & Hu, H. (2012). Cellulose acetate fibers covered by CdS nanoparticles for hybrid solar cell applications. *Materials Science and Engineering: B*, *177*(16), 1491–1496. https://doi.org/10.1016/j.mseb.2012.02.014

Dang, M. T., Hirsch, L., & Wantz, G. (2011). P3HT:PCBM, best seller in polymer photovoltaic research. *Advanced Materials*, *23*(31), 3597–3602. https://doi.org/10.1002/adma.201100792

Deka, K., & Kalita, M. P. C. (2018). Structural phase controlled transition metal (Fe, Co, Ni, Mn) doping in CdS nanocrystals and their optical, magnetic and photocatalytic properties. *Journal of Alloys and Compounds*, *757*, 209–220. https://doi.org/10.1016/j.jallcom.2018.04.323

Demirselcuk, B., Kus, E., Kucukarslan, A., Sarica, E., Akyuz, I., & Bilgin, V. (2021). Optimization of chemically sprayed ZnS films by Mn doping. *Physica B: Condensed Matter*, *622*. https://doi.org/10.1016/j.physb.2021.413353

Deng, K., & Li, L. (2014). CdS nanoscale photodetectors. *Advanced Materials*, *26*(17), 2619–2635. https://doi.org/10.1002/adma.201304621

Devi, L. S., Devi, K. N., Sharma, B. I., & Sarma, H. N. (2014). Influence of Mn doping on structural and optical properties of CdS nanoparticles. *Indian Journal of Physics*, *88*(5), 477–482. https://doi.org/10.1007/s12648-013-0436-8

Dive, A. S., Gattu, K. P., Huse, N. P., Upadhayay, D. R., Phase, D. M., & Sharma, R. B. (2018). Single step chemical growth of ZnMgS nanorod thin film and its DFT study. *Materials Science and Engineering B: Solid-State Materials for Advanced Technology*, *228*, 91–95. https://doi.org/10.1016/j.mseb.2017.11.018

Du, L., Zhang, Y., Lei, Y., & Zhao, H. (2014). Synthesis of high-quality CdS nanowires and their application as humidity sensors. *Materials Letters*, *129*, 46–49. https://doi.org/10.1016/j.matlet.2014.05.002

El-Shaer, A., Ezzat, S., Habib, M. A., Alduaij, O. K., Meaz, T. M., & El-Attar, S. A. (2023). Influence of Deposition Time on Structural, Morphological, and Optical Properties of CdS Thin Films Grown by Low-Cost Chemical Bath Deposition. *Crystals*, *13*(5). https://doi.org/10.3390/cryst13050788

Firoozi, N., Dehghani, H., & Afrooz, M. (2015). Cobalt-doped cadmium sulfide nanoparticles as efficient strategy to enhance performance of quantum dot sensitized solar cells. *Journal of Power Sources*, *278*, 98–103. https://doi.org/10.1016/j.jpowsour.2014.12.033

Gadalla, A., Almokhtar, M., & Abouelkhir, A. N. (2018). EFFECT OF Mn DOPING ON STRUCTURAL, OPTICAL AND MAGNETIC PROPERTIES OF CdS DILUTED MAGNETIC SEMICONDUCTOR NANOPARTICLES. In *Chalcogenide Letters* (Vol. 15, Issue 4).

Ganguly, A., & Nath, S. S. (2020). Mn-doped CdS quantum dots as sensitizers in solar cells. *Materials Science and Engineering: B*, *255*. https://doi.org/10.1016/j.mseb.2020.114532

Giribabu, G., Murali, G., Amaranatha Reddy, D., Liu, C., & Vijayalakshmi, R. P. (2013). Structural, optical and magnetic properties of Co doped CdS nanoparticles. *Journal of Alloys and Compounds*, *581*, 363–368. https://doi.org/10.1016/j.jallcom.2013.07.082

Girish, M., Sivakumar, R., & Sanjeeviraja, C. (2021). Tuning the properties of Cd1-xMnxS films deposited by nebulized spray pyrolysis. *Optik*, *227*. https://doi.org/10.1016/j.ijleo.2020.166088

Gupta, A. K., & Kripal, R. (2012). EPR and photoluminescence properties of Mn2+ doped CdS nanoparticles synthesized via co-precipitation method. *Spectrochimica Acta - Part A: Molecular and Biomolecular Spectroscopy*, *96*, 626–631. https://doi.org/10.1016/j.saa.2012.07.038

Hau, S. K., Yip, H. L., & Jen, A. K. Y. (2010). A review on the development of the inverted polymer solar cell architecture. In *Polymer Reviews* (Vol. 50, Issue 4, pp. 474–510). https://doi.org/10.1080/15583724.2010.515764

Hiie, J., Dedova, T., Valdna, V., & Muska, K. (2006). Comparative study of nano-structured CdS thin films prepared by CBD and spray pyrolysis: Annealing effect. *Thin Solid Films*, *511–512*, 443–447. https://doi.org/10.1016/j.tsf.2005.11.070

Huang, Y. J., Lo, W. C., Liu, S. W., Cheng, C. H., Chen, C. T., & Wang, J. K. (2013). Unified assay of adverse effects from the varied nanoparticle hybrid in polymer-fullerene organic photovoltaics. *Solar Energy Materials and Solar Cells*, *116*, 153–170. https://doi.org/10.1016/j.solmat.2013.03.031

Ibraheem, F., Mahdy, M. A., Mahmoud, E. A., Ortega, J. E., Rogero, C., Mahdy, I. A., & El-Sayed, A. (2020). Tuning Paramagnetic effect of Co-Doped CdS diluted magnetic

semiconductor quantum dots. *Journal of Alloys and Compounds*, *834*. https://doi.org/10.1016/j.jallcom.2020.155196

Jabeen, U., Adhikari, T., Pathak, D., Shah, S. M., & Nunzi, J. M. (2018). Structural, optical and photovoltaic properties of P3HT and Mn-doped CdS quantum dots based bulk hetrojunction hybrid layers. *Optical Materials*, *78*, 132–141. https://doi.org/10.1016/j.optmat.2018.02.019

Jadhav, P. A., Panmand, R. P., Patil, D. R., Fouad, H., Gosavi, S. W., & Kale, B. B. (2017). Triangular CdS nanostructure: effect of Mn doping on photoluminescence, electron spin resonance, and magneto-optical properties. *Journal of Nanoparticle Research*, *19*(6). https://doi.org/10.1007/s11051-017-3903-x

Jassim, S. A. J., Zumaila, A. A. R. A., & Waly, G. A. A. Al. (2013). Influence of substrate temperature on the structural, optical and electrical properties of CdS thin films deposited by thermal evaporation. *Results in Physics*, *3*, 173–178. https://doi.org/10.1016/j.rinp.2013.08.003

Ji, X., Li, H., Cheng, S., Wu, Z., Xie, Y., Dong, X., & Yan, P. (2011). Growth and photoluminescence of CdS and CdS:Mn Nanoribbons. *Materials Letters*, *65*(17–18), 2776–2778. https://doi.org/10.1016/j.matlet.2011.06.003

Kadem, B. Y., Al-Hashimi, M., Hasan, A. S., Kadhim, R. G., Rahaq, Y., & Hassan, A. K. (2018). The effects of the PEDOT:PSS acidity on the performance and stability of P3HT:PCBM-based OSCs. *Journal of Materials Science: Materials in Electronics*, *29*(22), 19287–19295. https://doi.org/10.1007/s10854-018-0055-4

Kathirvel, D., Suriyanarayanan, N., Prabahar, S., Srikanth, S., & Rajasekaran, P. (2011). STRUCTURAL, OPTICAL AND ELECTRICAL PROPERTIES OF CHEMICAL BATH DEPOSITED CdS THIN FILMS. In *Chalcogenide Letters* (Vol. 8, Issue 12).

Kaur, K., Lotey, G. S., & Verma, N. K. (2013). Structural, optical and magnetic properties of cobalt-doped CdS dilute magnetic semiconducting nanorods. *Materials Chemistry and Physics*, *143*(1), 41–46. https://doi.org/10.1016/j.matchemphys.2013.08.005

Khallaf, H., Oladeji, I. O., Chai, G., & Chow, L. (2008). Characterization of CdS thin films grown by chemical bath deposition using four different cadmium sources. *Thin Solid Films*, *516*(21), 7306–7312. https://doi.org/10.1016/j.tsf.2008.01.004

Korte, D., Pavlica, E., Klančar, D., Bratina, G., Pawlak, M., Gondek, E., Song, P., Liu, J., & Derkowska-Zielinska, B. (2023). Influence of P3HT:PCBM Ratio on Thermal and Transport Properties of Bulk Heterojunction Solar Cells. *Materials*, *16*(2). https://doi.org/10.3390/ma16020617

Kumar, S., Sharma, P., & Sharma, V. (2014). Redshift in absorption edge of Cd1-xCoxS nanofilms. *IEEE Transactions on Nanotechnology*, *13*(2), 343–348. https://doi.org/10.1109/TNANO.2014.2303200

Li, T., Zou, X., & Zhou, H. (2014). Erratum: Effect of Mn doping on properties of CdS quantum dot-sensitized solar cells (International Journal of Photoenergy). *International Journal of Photoenergy*, *2014*. https://doi.org/10.1155/2014/569763

Maity, P., Singh, S. V., Biring, S., Pal, B. N., & Ghosh, A. K. (2019). Selective near-infrared (NIR) photodetectors fabricated with colloidal CdS:Co quantum dots. *Journal of Materials Chemistry C*, *7*(25), 7725–7733. https://doi.org/10.1039/c9tc01871a

Martínez-Landeros, V. H., Hernandez-Como, N., Gutierrez-Heredia, G., Quevedo-Lopez, M. A., & Aguirre-Tostado, F. S. (2019). Structural, chemical and electrical properties of CdS thin films fabricated by pulsed laser deposition using varying background gas pressure. *Thin Solid Films*, *682*, 24–28. https://doi.org/10.1016/j.tsf.2019.05.014

McLeod, J. A., Pitman, A. L., Kurmaev, E. Z., Finkelstein, L. D., Zhidkov, I. S., Savva, A., & Moewes, A. (2015). Linking the HOMO-LUMO gap to torsional disorder in P3HT/PCBM blends. *Journal of Chemical Physics*, *143*(22). https://doi.org/10.1063/1.4936898

Mercy, A., Jesper Anandhi, A., Sakthi Murugesan, K., Jayavel, R., Kanagadurai, R., & Milton Boaz, B. (2014). Synthesis, structural and property studies of Ni doped cadmium sulphide quantum dots stabilized in DETA matrix. *Journal of Alloys and Compounds*, *593*, 213–219. https://doi.org/10.1016/j.jallcom.2013.12.161

Muruganandam, S., Anbalagan, G., & Murugadoss, G. (2015). Optical, electrochemical and thermal properties of Co2+-doped CdS nanoparticles using polyvinylpyrrolidone. *Applied Nanoscience (Switzerland)*, *5*(2), 245–253. https://doi.org/10.1007/s13204-014-0313-6

Murugesan, R., Sivakumar, S., Karthik, K., Anandan, P., & Haris, M. (2019). Effect of Mg/Co on the properties of CdS thin films deposited by spray pyrolysis technique. *Current Applied Physics*, *19*(10), 1136–1144. https://doi.org/10.1016/j.cap.2019.07.008

Pitchaimani, K., Amalraj, L., & Muthukumaran, S. (2016). Investigation of structural, photoluminescence and antibacterial behavior of Mn-doped and Co, Mn dual doped CdS thin films by CBD method. *Journal of Materials Science: Materials in Electronics*, *27*(11), 12021–12027. https://doi.org/10.1007/s10854-016-5350-3

Prabahar, S., & Dhanam, M. (2005). CdS thin films from two different chemical baths - Structural and optical analysis. *Journal of Crystal Growth*, *285*(1–2), 41–48. https://doi.org/10.1016/j.jcrysgro.2005.08.008

Pradeep, C., Mathew, S., Namboothiry, M. A. G., Vallabhan, C. P. G., Radhakrishnan, P., & Nampoori, V. P. N. (2016). Performance of polymer/CdS organic-inorganic hybrid LEDs. *Optoelectronics Letters*, *12*(2), 110–114. https://doi.org/10.1007/s11801-016-5220-5

Ruiz-Ortega, R. C., Esquivel-Mendez, L. A., Gonzalez-Trujillo, M. A., Hernandez-Vasquez, C., Matsumoto, Y., & Albor-Aguilera, M. de L. (2023). Comprehensive Analysis of CdS Ultrathin Films Modified by the Substrate Position inside the Reactor Container Using the CBD Technique. *ACS Omega*. https://doi.org/10.1021/acsomega.3c02158

Sahu, N., & Panigrahi, S. (2009). Fundamental understanding and modeling of spin coating process : A review. In *Indian J. Phys* (Vol. 83, Issue 4).

Salzmann, I., Heimel, G., Oehzelt, M., Winkler, S., & Koch, N. (2016). Molecular Electrical Doping of Organic Semiconductors: Fundamental Mechanisms and Emerging Dopant Design Rules. In *Accounts of Chemical Research* (Vol. 49, Issue 3, pp. 370–378). American Chemical Society. https://doi.org/10.1021/acs.accounts.5b00438

Saravanan, L., Pandurangan, A., & Jayavel, R. (2011). Synthesis of cobalt-doped cadmium sulphide nanocrystals and their optical and magnetic properties. *Journal of Nanoparticle Research*, *13*(4), 1621–1628. https://doi.org/10.1007/s11051-010-9915-4

Shaban, M., Elwahab, F. A., Ghitas, A. E., & El Zayat, M. Y. (2020). Efficient and recyclable photocatalytic degradation of methylene blue dye in aqueous solutions using nanostructured Cd1 − xCoxS films of different doping levels. *Journal of Sol-Gel Science and Technology*, *95*(2), 276–288. https://doi.org/10.1007/s10971-020-05331-x

Shi, H., Liu, C., Jiang, Q., & Xu, J. (2015). Effective Approaches to Improve the Electrical Conductivity of PEDOT:PSS: A Review. *Advanced Electronic Materials*, *1*(4). https://doi.org/10.1002/aelm.201500017

Suo, Z., Dai, J., Gao, S., & Gao, H. (2020). Effect of transition metals (Sc, Ti, V, Cr and Mn) doping on electronic structure and optical properties of CdS. *Results in Physics*, *17*. https://doi.org/10.1016/j.rinp.2020.103058

Thitima, R., Patcharee, C., Takashi, S., & Susumu, Y. (2009). Efficient electron transfers in ZnO nanorod arrays with N719 dye for hybrid solar cells. *Solid-State Electronics*, *53*(2), 176–180. https://doi.org/10.1016/j.sse.2008.10.014

Tomakin, M., Öncel, Y., Keskenler, E. F., Nevruzoğlu, V., Onuk, Z., & Görür, O. (2014). Investigation of Cd1-xCoxS diluted magnetic semiconductor thin films fabricated by chemical bath deposition method. *Journal of Alloys and Compounds*, *616*, 166–172. https://doi.org/10.1016/j.jallcom.2014.07.139

Tyagi, V. V., Rahim, N. A. A., Rahim, N. A., & Selvaraj, J. A. L. (2013). Progress in solar PV technology: Research and achievement. In *Renewable and Sustainable Energy Reviews* (Vol. 20, pp. 443–461). Elsevier Ltd. https://doi.org/10.1016/j.rser.2012.09.028

Wondmagegn, W., Mejia, I., Salas-Villasenor, A., Stiegler, H. J., Quevedo-Lopez, M. A., Pieper, R. J., & Gnade, B. E. (2016). CdS Thin Film Transistor for Inverter and Operational Amplifier Circuit Applications. *Microelectronic Engineering*, *157*, 64–70. https://doi.org/10.1016/j.mee.2016.02.042

Wright, M., & Uddin, A. (2012). Organic-inorganic hybrid solar cells: A comparative review. In *Solar Energy Materials and Solar Cells* (Vol. 107, pp. 87–111). https://doi.org/10.1016/j.solmat.2012.07.006

Xie, S., Li, X., Jiang, Y., Yang, R., Fu, M., Li, W., Pan, Y., Qin, D., Xu, W., & Hou, L. (2020). Recent progress in hybrid solar cells based on solution-processed organic and semiconductor nanocrystal: Perspectives on device design. In *Applied Sciences (Switzerland)* (Vol. 10, Issue 12). MDPI AG. https://doi.org/10.3390/app10124285

Yavuz, N., Yuksel, S. A., Karsli, A., & Gunes, S. (2013). Inverted structure hybrid solar cells using CdS thin films. *Solar Energy Materials and Solar Cells*, *116*, 224–230. https://doi.org/10.1016/j.solmat.2013.04.018

Yılmaz, S., Polat, I., Olgar, M. A., Tomakin, M., Töreli, S. B., & Bacaksız, E. (2017). Physical properties of CdS:Ga thin films synthesized by spray pyrolysis technique. *Journal of Materials Science: Materials in Electronics*, *28*(4), 3191–3199. https://doi.org/10.1007/s10854-016-5908-0

Yılmaz, S., Tomakin, M., Ünverdi, A., Aydın, A., Polat, I., & Bacaksız, E. (2020). Structural, morphological, optical analyses of Ni-doped CdS thin films and their photovoltaic performance in hybrid solar cells. *Journal of Materials Science: Materials in Electronics*, *31*(15), 12932–12942. https://doi.org/10.1007/s10854-020-03846-1

Yılmaz, S., Ünverdi, A., Tomakin, M., Altay, M., Polat, İ., & Bacaksız, E. (2020). Exploration of impact of Cr-doping on physical and optical properties of CdS thin films in hybrid photovoltaic cells. *Turk. J. Mater*, *5*(1), 1–9. http://www.sloi.org/sloi-name-of-this-article

Yılmaz, S., Ünverdi, A., Tomakin, M., Polat, & Bacaksız, E. (2019). Surface modification of CBD-grown CdS thin films for hybrid solar cell applications. *Optik*, *185*, 256–263. https://doi.org/10.1016/j.ijleo.2019.03.156